iScience

CellPress
OPEN ACCESS

Article

Ni-Ru supported on CeO_2 obtained by mechanochemical milling for catalytic hydrogen production from ammonia

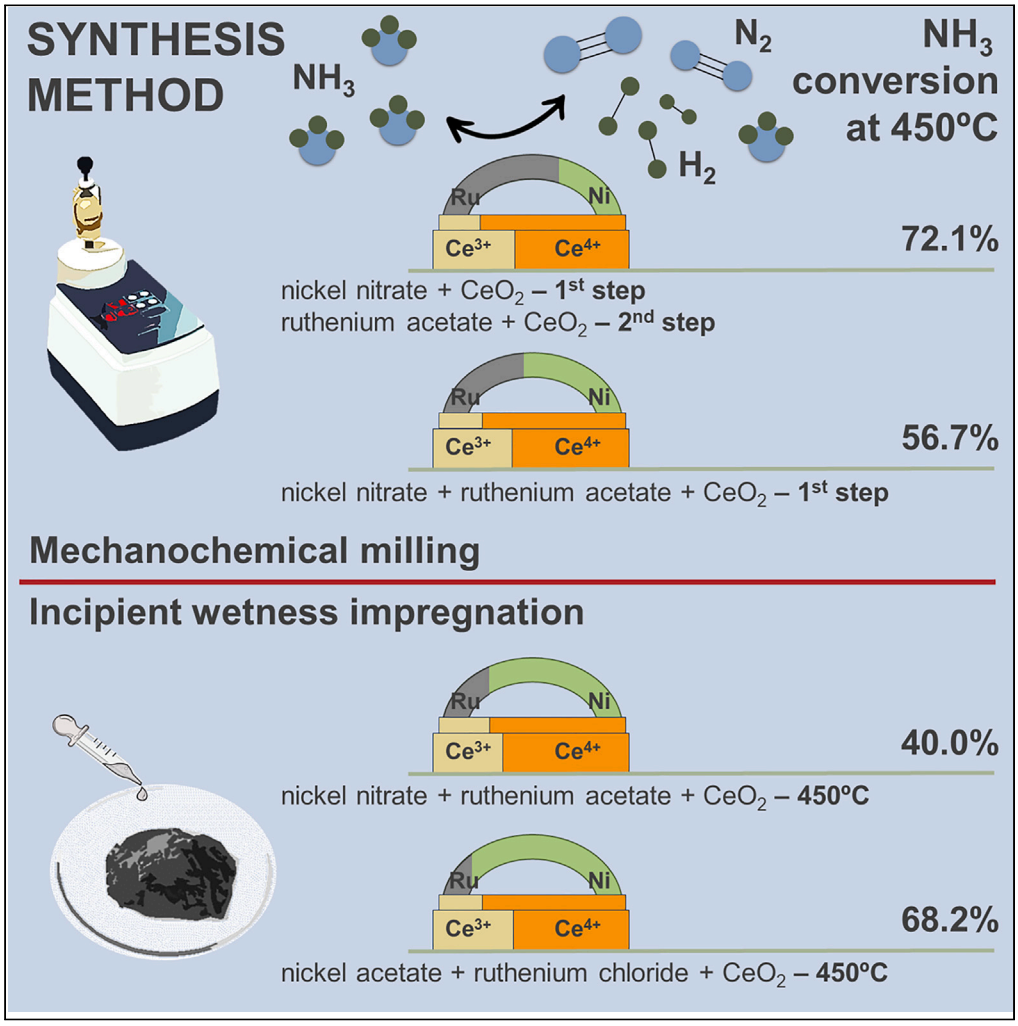

Ilaria Lucentini, Isabel Serrano, Xènia Garcia, ..., Carlo Marini, Carlos Escudero, Jordi Llorca

cescudero@cells.es (C.E.)
jordi.llorca@upc.edu (J.L.)

Highlights

Mechanochemical synthesis is an efficient method for catalyst preparation

$NiRu/CeO_2$ has proven to be a highly active catalyst for NH_3 decomposition

The high activity is attributed to a high number of vacancies in CeO_2 structure

Lucentini et al., iScience 27, 110028
June 21, 2024
https://doi.org/10.1016/j.isci.2024.110028

iScience

CellPress
OPEN ACCESS

Article

Ni-Ru supported on CeO_2 obtained by mechanochemical milling for catalytic hydrogen production from ammonia

Ilaria Lucentini,[1,2] Isabel Serrano,[1] Xènia Garcia,[1] Alba Garzón Manjón,[3] Xinxin Hu,[3] Jordi Arbiol,[3,4] Laia Pascua-Solé,[1] Jordi Prat,[2] Edgar Eduardo Villalobos-Portillo,[2] Carlo Marini,[2] Carlos Escudero,[2,*] and Jordi Llorca[1,5,*]

SUMMARY

Developing active and stable catalysts for carbon-free hydrogen production is crucial to mitigate the effects of climate change. Ammonia is a promising carbon-free hydrogen source, as it has a high hydrogen content and is liquid at low pressure, which allows its easy storage and transportation. We have recently developed a nickel-based catalyst with a small content of ruthenium supported on cerium oxide, which exhibits high activity and stability in ammonia decomposition. Here, we investigate mechanochemical milling for its synthesis, a faster and less energy-consuming technique than conventional ones. Results indicate that mechanochemical synthesis increases catalytic activity compared to the conventional incipient wetness impregnation method. The interaction between the metal precursors and the support is key in fine-tuning catalytic activity, which increases linearly with oxygen vacancies in the support. Moreover, the mechanochemical method modifies the oxidation state of Ni and Ru species, with a variation depending on the precursors.

INTRODUCTION

To limit climate change and environmental degradation, the European Commission approved the European Green Deal[1] in 2020. Among the suggested actions, the decarbonization of power generation is of prime importance, as it accounts for around three-quarters of global greenhouse gas emissions. In this context, hydrogen plays a key role. Its role has been described in detail in the Hydrogen Strategy,[2] which aims to develop and scale up renewable and low-carbon hydrogen supply and demand, turning hydrogen into a viable solution toward a climate-neutral economy. Among the proposed actions, the on-site catalytic production of hydrogen from ammonia is considered an interesting approach to feed proton exchange membrane fuel cells, which require a high hydrogen purity.[3] Among numerous advantages, ammonia, a carbon-free molecule, has a high hydrogen content (17.8 wt.% and 108 kg H_2 m^{-3} at 20°C and 8.6 bar[4]), and it can be stored and transported easily as it can liquefy at low pressure. It is decomposed catalytically into hydrogen and nitrogen at moderate temperature, around 400°C–600°C at 1 bar ($2NH_{3(g)} \leftrightarrows N_{2(g)} + 3H_{2(g)}$; $\Delta H° = 92$ kJ mol^{-1}, i.e., the ammonia decomposition).

Currently, research on the catalysts for ammonia decomposition, aimed at hydrogen production, still focuses on ruthenium, with nickel and cobalt emerging as primary alternatives due to their cost-effectiveness. Alternative preparation techniques, including coprecipitation[5] or sol-gel[6,7] methods, are being investigated, together with the effect of different promoters,[8–10] supports,[11,12] or active phase precursors[13] on the catalyst activity. Moreover, the utilization of oxide combinations, such as Al-La-Ce[14] or CeO_2-promoted $MgAl_2O_4$,[15] as catalyst supports, has allowed the enhancement of the stability of ruthenium, and this effect has been ascribed to the high presence of oxygen vacancies in the support structure. Innovative combinations based on aluminate,[16] zeolite,[17] or perovskite[18] structures and bimetallic catalysts such as Ni-Mo[19] and Fe-Cr[20] have also presented good results. We have recently developed a catalyst based on nickel (5 wt.%) with a small content of ruthenium (1 wt.%) supported on ceria nanoparticles for the ammonia decomposition prepared by classical incipient wetness impregnation (IWI), which showed an excellent catalytic performance in long-term stability tests with respect to monometallic Ru/CeO_2 and Ni/CeO_2 and in multicycle tests.[21] The bimetallic catalyst prepared did not allow an increase in the conversion obtained with Ru/CeO_2, but the latter deactivates rapidly (as demonstrated in a previous work[22]). The characterization has revealed the existence of an intimate contact between Ni, Ru, and CeO_2, which is considered the reason for the excellent catalytic activity and stability observed.[23]

[1]Institute of Energy Technologies, Department of Chemical Engineering and Barcelona Research Center in Multiscale Science and Engineering, Universitat Politècnica de Catalunya, EEBE, Eduard Maristany 10-14, 08019 Barcelona, Spain
[2]ALBA Synchrotron Light Source, Carrer de la Llum 2-26, 08290 Cerdanyola del Valles, Barcelona, Spain
[3]Catalan Institute of Nanoscience and Nanotechnology (ICN2), CSIC and BIST, Campus UAB, Bellaterra, 08193 Barcelona, Catalonia, Spain
[4]ICREA, Pg. Lluís Companys 23, 08010 Barcelona, Catalonia, Spain
[5]Lead contact
*Correspondence: cescudero@cells.es (C.E.), jordi.llorca@upc.edu (J.L.)
https://doi.org/10.1016/j.isci.2024.110028

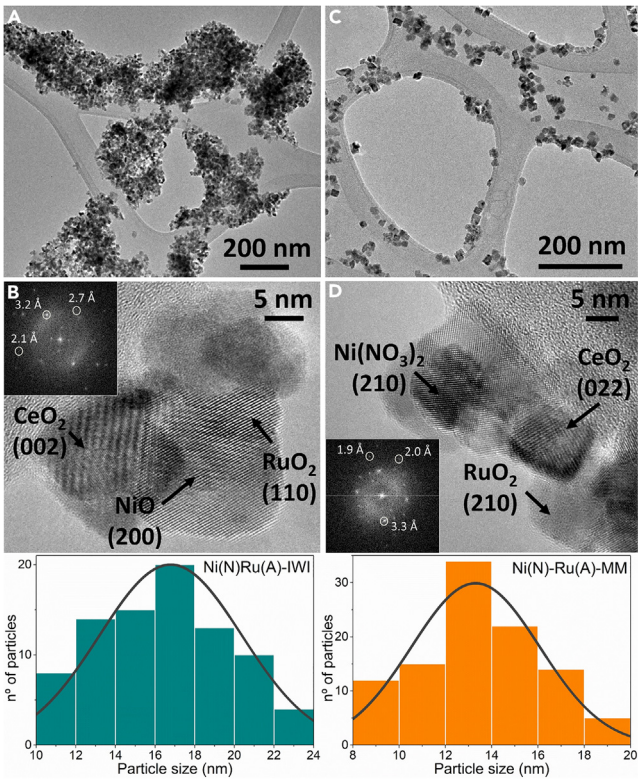

Figure 1. HRTEM images of bimetallic samples Ni(N)-Ru(A)-IWI and Ni(N)-Ru(A)-MM

(A and B) Ni(N)-Ru(A)-IWI and (C and D) Ni(N)-Ru(A)-MM, with the histograms of particle size.

The method employed to synthesize the catalysts, IWI, is widely used, although nowadays alternative technologies, such as mechanochemical milling (MM), are being investigated to precisely control the active sites formation according to specific properties of amorphous/crystalline interfaces. MM synthesis methods are particularly attractive due to their low energy and time requirements, versatility, and scalability. The possibility of preparing materials with an amorphous layer on the support using MM methods has been already reported in the literature.[24] It has been observed that the formation of the amorphous phase increases as the milling time increases. This phenomenon has been attributed to the fact that the energy stored as structural defects[25,26] on the surface of the particles becomes greater than in the bulk; therefore, to minimize the energy, an amorphous phase or thin layer can form on the surface or at the edges of the particles, while maintaining the elementary crystalline matrix.[25] In previous works,[27–30] the described amorphous layer was obtained using the MM method with different catalysts supported on ceria, and it has been demonstrated that the formation of this amorphous layer is closely linked to an increase in the activity of the catalyst. However, it is not always possible to obtain this amorphous/crystalline interface, as it strongly depends on the relative hardness of the precursors. Nonetheless, the amorphization of a part of the supported metal, using Ni or Ru, has been reported in the literature.[31,32]

In this work, we study the MM method for the synthesis of the bimetallic catalyst composed of 5 wt.% of Ni and 1 wt.% of Ru supported on ceria. The aim is to reduce the time and energy required for the catalyst preparation while increasing the repeatability of the synthesis procedure. In particular, we have varied the precursors of the two metals among different forms (nitrate: N, acetate: A, chloride: C, and nanoparticles: np). Additionally, we have studied the effect on the catalyst activity of the introduction of the precursors into the MM vial in one or two steps (denoted by the absence or the presence of a line between the two precursors, starting with the precursor used in the first phase, respectively), to identify the synthesis procedure that maximizes the activity in ammonia decomposition for hydrogen production. Furthermore, through the characterization we establish correlations between catalyst characteristics and the synthesis method, comparing IWI and MM methods, while identifying the relationship between the precursor used and the resulting catalyst's properties. Specifically, we focus on the presence of defects within the ceria structure, on the oxidation states of Ni and Ru, and on the dispersion of these on the surface of the catalyst.

RESULTS

Morphological properties of the catalysts

HRTEM was employed to study the morphology, particle size, and crystal structure of catalysts prepared using the same precursors with the two different methods (Ni(N)Ru(A)-IWI and Ni(N)-Ru(A)-MM; Figure 1). The ceria particles that compose the analyzed catalysts exhibited an

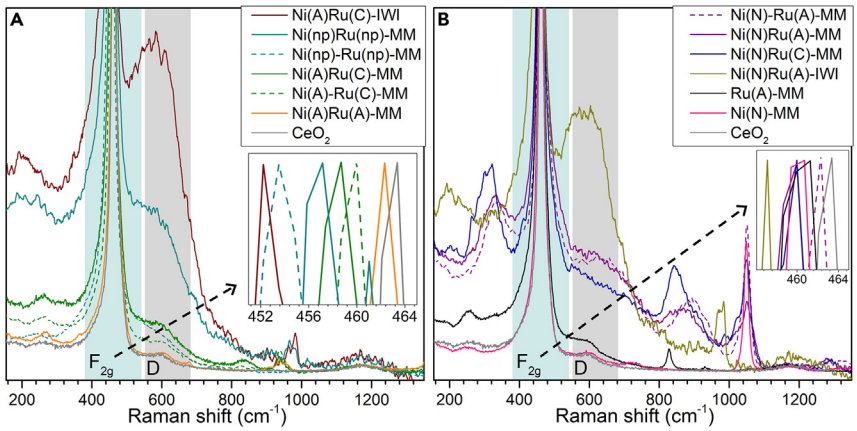

Figure 2. Raman spectra of the samples as prepared

(A) Those prepared with Ni(A) and Ni(np) as precursors, and (B) those prepared with Ni(N) as precursor and monometallic samples. The inserts show the F_{2g} peak center for all the catalysts and the bare support.

average size of around 17 ± 4 nm for the catalyst prepared by IWI and 13 ± 3 nm for the one prepared by MM method, as determined from the histograms (Figure 1) obtained by measuring the particles in Figures 1A and 1C. In the high-resolution images (Figures 1B and 1D), differences in the d-spacing identified in the FFT images (insets) can be observed. In the case of the IWI catalyst, besides the identified planes attributed to cerium oxide [mainly (111), (002), (022), and (113) identified through d-spacing of 3.1, 2.7, 1.9, and 1.6 Å, respectively], d-spacings corresponding to the oxidized forms of Ni and Ru were identified as well, in particular, the planes (110) with a d-spacing of 3.2 Å; (210), 2.0 Å; and (211), 1.7 Å of RuO_2[33] and the planes (111) (d-spacing of 2.4 Å) and (200), 2.1 Å, of NiO.[34] It was not possible to estimate the average dimensions of the NiO and RuO_2 particles because their crystallites overlap with those of the ceria. This indicates that the particles of the two oxides and the support are intimately interconnected within the catalyst structure. For the MM-prepared catalyst, crystalline (210) planes of $Ni(NO_3)_2$ with a d-spacing of 3.3 Å[35] were identified. Similarly, these planes overlapped with ceria crystallites, hindering the unequivocal identification of the particles. No interplanar distances related to ruthenium acetate have been identified; however, d-spacings attributable to RuO_2 were identified, specifically at 3.2, 2.6, 2.0, and 1.7 Å corresponding to the (110), (101), (210), and (211) planes.

Interaction between the active phase and the support

The Raman spectra of the prepared catalysts are presented in Figure 2. The bands at 265, 463, 591, and 1177 cm^{-1} observed in the bare ceria spectrum are assigned to the second-order transverse acoustic (2TA) mode, the vibrational mode of the fluorite phase (F_{2g}), the defect-induced mode (D), and the second-order longitudinal optical (2LO) mode, respectively.[36] All spectra were normalized to the height of the F_{2g} peak. These bands were observed in all spectra, with certain variations: a broadening coupled with a red shift of the F_{2g} peak, and an increase in the area of the bands related to defects in the ceria structure were observed for all the supported catalysts. These variations are linked to decreasing mean crystallite size, increasing lattice parameters, and higher disorder in the ceria structure.[37] In particular, a more pronounced red shift and broadening of the F_{2g} peak, and a larger area of the D and 2TA mode bands, indicate a higher level of defects in the ceria structure. The D band associated with defects in the ceria structure can be divided into three contributions: D1, due to intrinsic Frenkel defects of ceria; D2, due to extrinsic defects originating from metal-support interaction; and D3, assigned to oxygen vacancies coupled to the presence of Ce^{3+} or other aliovalent cations.[38] The ratio between the F_{2g} band area and the sum of the areas of three contributions D1, D2, and D3 (D) is indicative of the interaction between the support and the used precursors. The values of the F_{2g} peak center, its FWHM, and the ratio between the intensity of the D band and that of F_{2g} (I_D/I_F) for all the prepared catalysts and the support are reported in Table 1. In addition to the ceria oxide bands, several additional bands were observed in the spectra of the prepared catalysts. Catalysts synthesized using nickel acetate displayed peaks related to the presence of carbon and/or oxygen bonds, in particular, a peak at 952 cm^{-1}, attributed to ν_4(C-C) and one at 680 cm^{-1}, assigned to ν_5(COO). In addition to these peaks, the spectra of the catalysts prepared using Ni acetate presented peaks at 364 and 270 cm^{-1}, corresponding to the stretching vibration of ν(Ni-O) of the aquo complex of Ni(II) and of the acetate-nickel complex,[39] respectively. In the case of the Ni(A)Ru(A) catalyst, the peak at 952 cm^{-1} overlapped with a second peak (936 cm^{-1}), attributed to the presence of Ru acetate, as confirmed by analyzing the Ru(A)-MM catalyst spectrum (Figure 2B) where this peak appears at 930 cm^{-1} (attributed to ν(C–C) of Ru acetate). In the Ru(A)-MM spectrum, a band around 334–338 cm^{-1} is visible, ascribed to hydrated RuO_2,[40] and this band is stronger in the spectra of the catalysts prepared using Ru(A) and Ni(N) as precursors. Furthermore, in the case of the monometallic catalyst Ru(A)-MM, a peak at 828 cm^{-1} was identified, which is not visible in the spectrum of Ni(A)Ru(A)-MM. Bimetallic spectra containing Ru(A) also displayed a band around 900 cm^{-1}. These bands cannot be univocally attributed to a specific vibrational mode but likely originate from ruthenium acetate's presence or its interaction with the Ni precursor or ceria support. The analysis of the spectra of the catalysts prepared using Ru chloride as a precursor, apart from the peaks already described, revealed the presence of bands with peaks around 323 cm^{-1} (attributed to a quasi-elastic scattering component in A_{1g} of $RuCl_3$[41,42]) and 835–843 cm^{-1} (not unequivocally

Table 1. Properties of the catalysts associated with defects in the ceria structure

	Raman			*XANES*[a]	*XPS*	
Sample	F_{2g} cm^{-1}	FWHM F_{2g}	I_D/I_F	% Ce^{3+}/Ce	% Ce^{3+}/Ce	% O_S/O
CeO_2	463.4	14.9	0.04	16.4(3)	–	–
Ni(A)Ru(A)-MM	462.3	16.9	0.04	16.9(5)	–	–
Ni(A)-Ru(C)-MM	460.0	19.2	0.07	17.3(2)	–	–
Ni(N)-MM	460.7	16.0	0.04	20.6(6)	14.0	37.7
Ni(N)-IWI	–	–	–	21.6(6)	33.4	68.0
Ni(np)-Ru(np)-MM	453.5	35.6	0.09	23.0(2)	–	–
RuA-IWI	–	–	–	23.7(1)	–	–
RuA-MM	461.3	21.4	0.06	24.1(1)	–	–
Ni(A)Ru(C)-MM	458.7	22.6	0.10	24.3(6)	–	–
Ni(N)Ru(A)-IWI	457.1	33.6	0.69	24.9(1)	19.8	76.2
Ni(np)Ru(np)-MM	457.1	38.0	0.46	28.3(8)	–	–
Ni(N)Ru(C)-MM	460.0	21.8	0.16	29.8(1)	–	–
Ni(N)Ru(A)-MM	460.0	26.2	0.44	29.8(2)	17.9	40.5
Ni(N)-Ru(A)-MM	462.3	21.3	0.45	31.3(6)	16.2	42.7
Ni(A)Ru(C)-IWI	452.2	51.2	1.04	32.1(1)	18.1	25.5

[a]Uncertainty (Least Squares Method) is given in parentheses.

attributable to a specific vibrational mode, but likely resulting from the presence of Ru chloride). In the case of the catalysts prepared with $Ni(NO_3)_2.6H_2O$, a strong band between 1,010 and 1,080 cm^{-1}, corresponding to the nitrate group $v_1(NO^{3-})$, was observed. This band is composed of two peaks: one relative to the coordinated NO^{3-} at around 1,020 cm^{-1} and a second relative to the free NO^{3-} at around 1,050 cm^{-1}.[43] Monometallic Ni(N)-MM presented only the free NO^{3-}- related band, whereas the other Ni-nitrate-containing catalysts exhibited both contributions in a coordinated/free proportion of approximately 1/3 for Ni(N)Ru(C)-MM and Ni(N)Ru(A)-MM and around 1/5 for Ni(N)-Ru(A)-MM. Three weaker bands between 1,260–1,350; 700–760; and 400–420 cm^{-1}, corresponding to the stretching modes of v_{as}(NO), $v_4(NO^{3-})$ and v(Ni-N), respectively,[44,45] were detected. The spectra of the catalysts prepared by MM using Ni(np) and Ru(np) as precursors presented a pattern very similar to those of the two catalysts prepared by IWI: the D band was much more intense than for the other catalysts [especially intense for IWI catalysts and then for Ni(np)Ru(np)-MM], and the only peak observable, apart from the bands related to cerium oxide, around 965–975 cm^{-1}, coupled with a peak around 680–700 cm^{-1}, was attributed to the formation of the Ru-*O*-Ce bond.[46–48] The bands related to NiO and Ni-Ce-O are located at 520 and 635 cm^{-1}, respectively.[49] Therefore, in the samples examined they can be overlapped by the F_{2g} and D bands of ceria and consequently not distinguishable.

Composition of the catalysts and crystallite size

The X-ray diffraction (XRD) patterns of the prepared catalysts were collected at a wavelength of 0.05904 nm (21 keV) and are presented in Figure 3. All patterns present peaks attributed to cubic fluorite-type cerium oxide[50] with the four primary peaks identifiable at 2θ of 10.8° (111), 12.5° (200), 17.8° (220), and 20.9° (311). The dimensions of ceria crystallites calculated using the Debye-Scherrer equation are 11 nm in bare ceria and 12 nm for all prepared catalysts. No noticeable shift of the ceria-related peaks of the prepared catalysts compared to the CeO_2 pattern was identified. In the case of the catalysts prepared by IWI (Ni(N)Ru(A)-IWI and Ni(A)Ru(C)-IWI), peaks at 14.0° (111), 16.2° (200), and 23.0° (220) attributed to an FCC NiO phase[51] were observed, due to the calcination process at 450°C in the presence of air. Using the Debye-Scherrer equation the crystallite size of nickel oxide is estimated to be around 9 nm for both IWI catalysts. No ruthenium-related peaks were identified. The patterns of the catalysts prepared by MM method using Ni acetate as precursor presented several peaks related to Ni(A)[52] (dotted lines in Figure 3). This was confirmed through the analysis under the same conditions of the unsupported precursors (Figure 4). Ni(A) first peaks were observed at 2θ values of 4.9°, 5.7°, 7.1°, 7.7°, 8.0°, 8.4°, and 8.9°, corresponding to the peaks at 8.0°, 9.3°, 11.5°, 12.4°, 13.0°, 13.6°, and 13.8° of the unsupported Ni acetate, indicating that the peaks in the catalyst pattern have undergone a red shift. Using the Debye-Scherrer equation, the crystallite sizes of the highly crystalline unsupported material were estimated to be 59 nm, whereas in the case of the three prepared catalysts, these dimensions were estimated to be 50, 63, and 72 nm, in the order Ni(A)Ru(C)-MM < Ni(A)-Ru(C)-MM < Ni(A)Ru(A)-MM. In the XRD patterns of the catalysts prepared using the Ru chloride, Ru acetate, and Ni nitrate precursors, no peaks relative to Ru or Ni were identified. In the case of ruthenium, no considerations can be made as a content of 1 wt.% may be lower than the detection limit of the technique. In contrast, in the case of Ni, this may suggest that the particle size of Ni species is too small to be detected by XRD or that they are highly dispersed. Analyzing the unsupported precursors (Figure 4), Ru(C) main peaks were determined at 9.2°, 10.6°, 15.7°, and 21.4° 2θ angles,[53] and the dimensions of the crystallites were estimated to be around 10 nm, whereas in the case of Ru(A) the XRD pattern indicates a low

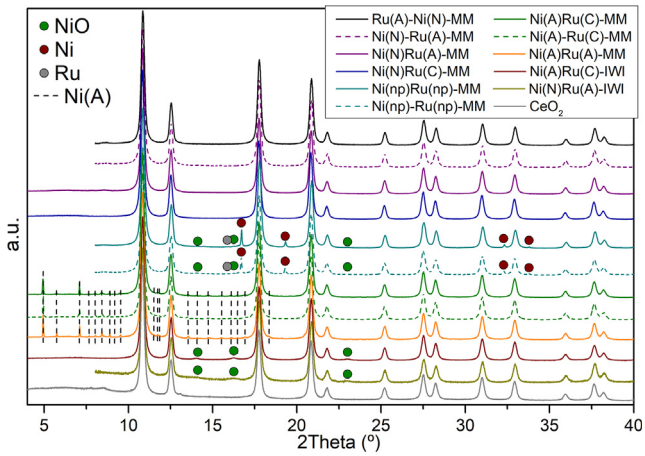

Figure 3. XRD patterns measured at 21 keV of the catalyst samples, as prepared

crystallinity level of the material. For catalysts prepared with Ni and Ru nanoparticles as precursors, the metallic FCC Ni (16.7°, 19.3°, 32.3°, and 33.8° 2θ angles) and HCP Ru (15.9° 2θ angle) phases were identified, along with the presence of Ni-oxidized phase in both analyzed catalysts. The size of the crystallites for the two highly crystalline precursors before being supported was estimated as 41 nm for metallic Ni [peaks 2θ located at 27.2° (111), 31.5° (200), 45.1° (220), 53.4° (311), and 56.0° (222)[54]] and 7 nm in the case of metallic Ru [main peak at 26.8° (101)[55]]. Also, in this case, a strong red shift of the peaks can be observed. When supported, the size of the Ni(np) crystalline increases to 48 nm in Ni(np) Ru(np)-MM and 51 nm in Ni(np)-Ru(np)-MM. The peaks related to the supported metallic Ru particles and NiO did not allow the estimation of the dimensions of their crystallites.

Oxygen vacancies in the ceria structure

The amount of Ce^{3+} ions compared to the total amount of ceria has been indicated as directly proportional to the number of oxygen defects present in its structure.[56] Therefore, to assess and quantify the valence states present in the support of the different prepared catalysts, X-ray absorption near edge structure (XANES) spectra were collected and analyzed. The raw data were reduced using *Athena*. A curve-fitting analysis was performed within the range of −25 and 25 eV with respect to the edge jump using an *arctan* function to simulate the edge jump (with a height of 0.95 and a width of 1.5, around 5726 eV) centered at the maximum of the first derivative.[57] All spectra exhibited the typical doublet due to the interaction between the 4f orbitals of the Ce atoms and the 2p orbitals of oxygen,[58,59] composed of four peaks (Figure 5A). Gaussian functions were employed to fit the peaks, centered around the energy values: 5721 (D), 5726 (C), 5731 (B), and 5738 eV (A). Component A is assigned to the transition from the Ce 2p shell to the 5d shell with no electron in the Ce 4f shell, whereaS component B is assigned to the excitation from the 2p shell to the 5d shell, along with an electron being excited from the O 2p shell to the Ce 4f shell, thus leaving a hole in the valence band. Components A and B are associated with the Ce^{4+} ions.[59] Component C, assigned to Ce^{3+}, results from the 5d to 4f emission.[60] Component D, in the pre-edge region, was assigned to the $2p_{3/2}$ to 4f quadrupole transition, which is a consequence of 5d ad-mixtures to the 4f states.[61] The quantification of [Ce^{3+}] was done by calculating the area ratio of Ce^{3+} (C) with respect to all Ce (A + B + C).[57] The results, reported in Table 1, indicate a variable presence of Ce^{3+}. The CeO_2 support presented an initial concentration of 16%, and the amount of reduced ceria increased with the presence of Ni and Ru, up to a maximum in the case of the Ni(N)-Ru(A)-MM and Ni(A)Ru(C)-IWI catalysts around 31% and 32%, respectively. In Figure 5B, the difference in intensity between the spectra of selected catalysts and the support is

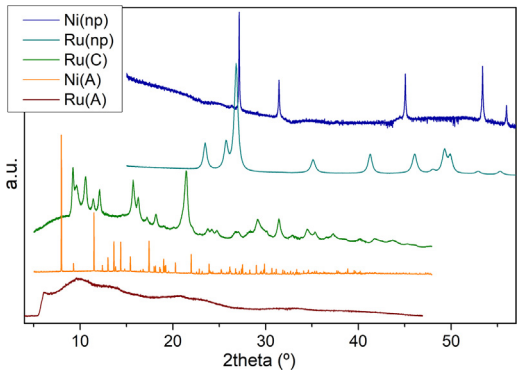

Figure 4. XRD patterns measured at 21 keV of the unsupported precursors

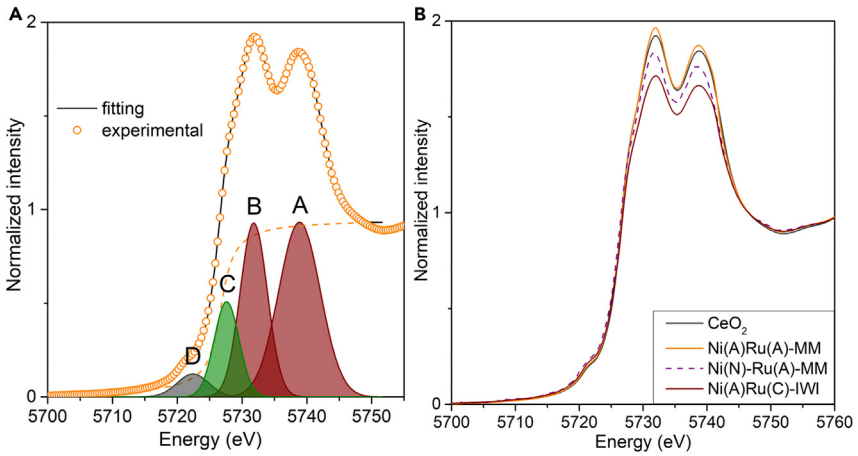

Figure 5. Normalized XANES spectra at the Ce L_3-edge for selected catalysts

(A) illustrates an example of fitting (CeO_2 bare support), whereas (B) presents a comparison of spectral intensity between CeO_2, Ni(A)Ru(A)-MM, Ni(N)-Ru(A)-MM, and Ni(A)Ru(C)-IWI.

observable: in Ni(A)Ru(A)-MM catalyst the estimated amount of reduced ceria remained unchanged compared to the support (16.9%), possibly indicating a low or absent interaction between the precursors, whereas in the case of the Ni(N)-Ru(A)-MM and Ni(A)Ru(C)-IWI catalysts a decrease in the Ce^{4+} contribution can be observed, indicated by the lower intensity of the doublets. These results support the findings from Raman spectroscopy: the MM method guarantees an excellent contact between Ni, Ru, and the support, since their presence leads to an increase in the presence of Ce^{3+}, associated with the presence of oxygen vacancies and defects in the ceria structure.

Oxidation state of the active phase

The XANES spectra collected at the K-edges of Ni and Ru were analyzed to identify their respective oxidation state. The obtained E_0 values for Ni (Figure 6A) and Ru (Figure 6B) are shown in Figure 6. These spectra revealed the presence of the oxidized forms in all catalysts prepared via MM. The percentage of NiO and RuO_2 obtained through linear combining fitting of the XANES spectra of the catalysts using those of the precursors and oxides is reported in Table 2. The catalysts prepared using nanoparticles of Ni and metallic Ru are mainly composed of the metallic form, with minor proportions of NiO [4.7 and 12.4% for Ni(np)-Ru(np)-MM and Ni(np)Ru(np)-MM, respectively] and RuO_2 [2.6 and 4.3% for Ni(np)-Ru(np)-MM and Ni(np)Ru(np)-MM, respectively]. The presence of RuO_2 is lower with respect to NiO, and in both EXAFS spectra the main contribution coincides with the spectrum of metallic form (Ni-Ni bond at 2.2 Å and Ru-Ru bond at 2.5 Å; Figures 7A and 8C). In contrast to catalysts employing metal nanoparticles, the analysis suggests a higher oxidation state of ruthenium compared to nickel in the other catalysts (Table 2). Generally, Ni acetate-based catalysts prepared via MM exhibited a lower fraction of the oxidized forms for both Ni and Ru. The IWI-prepared catalysts presented nearly complete oxidation of the precursors, particularly in the case of ruthenium, showing a 96%–98% oxide state according to the linear combination fitting of the XANES spectrum. Analyzing the magnitude of the FT, however, the IWI catalysts FT spectra (Figure 8D) lack the Ru oxide second shell peak (Ru–O–Ru) at 3.1 Å. This absence implies that the Ru species are likely anchored on the surface through Ru-*O*-Ce bonds, suggesting their presence as surface species rather than existing as RuO nanoclusters.[62] On the contrary, in the case of nickel, the spectrum exhibits both shells characteristic of Ni oxide (Figure 7D). This is supported by the Raman spectrum, wherein the presence of Ru-*O*-Ce bonds was identified in the catalysts prepared via IWI.

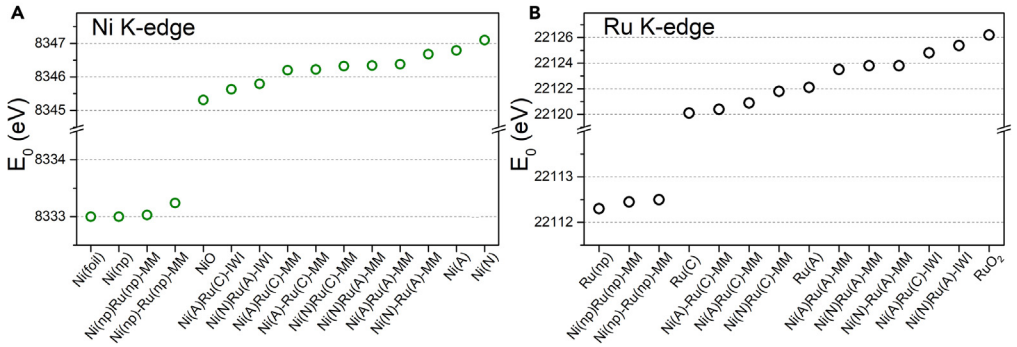

Figure 6. E_0 values obtained by analyzing XANES spectra of the catalysts prepared

(A) Ni K-edge and (B) Ru K-edge of the prepared catalysts.

Table 2. Properties associated with the active phase (Ni-Ru) of the prepared catalysts

	XRD		XANES[a]		XPS	
Sample	Form	Crystallite nm	% NiO	% RuO_2	% NiO/Ni	% RuO_2/Ru
Ni(np)-Ru(np)-MM	Ni(np)	51	4.7(1)	2.6(1)	–	–
Ni(np)Ru(np)-MM	Ni(np)	48	12.4(1)	4.3(1)	–	–
Ni(A)Ru(A)-MM	Ni(A)	72	6.7(2)	32.2(4)	–	–
Ni(A)-Ru(C)-MM	Ni(A)	63	10.3(2)	24.3(2)	–	–
Ni(A)Ru(C)-MM	Ni(A)	50	13.9(2)	26.6(2)	–	–
Ni(N)-Ru(A)-MM	–	–	26.5(3)	46.7(7)	59.9	31.1
Ni(N)Ru(C)-MM	–	–	34.7(4)	45.1(3)	–	–
Ni(N)Ru(A)-MM	–	–	32.5(4)	45.1(4)	49.7	56.1
Ni(A)Ru(C)-IWI	NiO	9	81.2(2)	93.6(2)	96.5	74.8
Ni(N)Ru(A)-IWI	NiO	9	96.2(3)	97.5(3)	92.4	63.7

[a]Uncertainty (Least Squares Method) is given in parentheses.

Surface atomic composition

XPS was employed to determine the surface composition of the catalysts. For the cerium 3d spectra, six peaks for Ce^{4+} (V, V″, V‴, U, U″, and U‴) were employed, representing three pairs of spin-orbit doublets, along with four peaks (two pairs of spin-orbit doublets) for Ce^{3+}

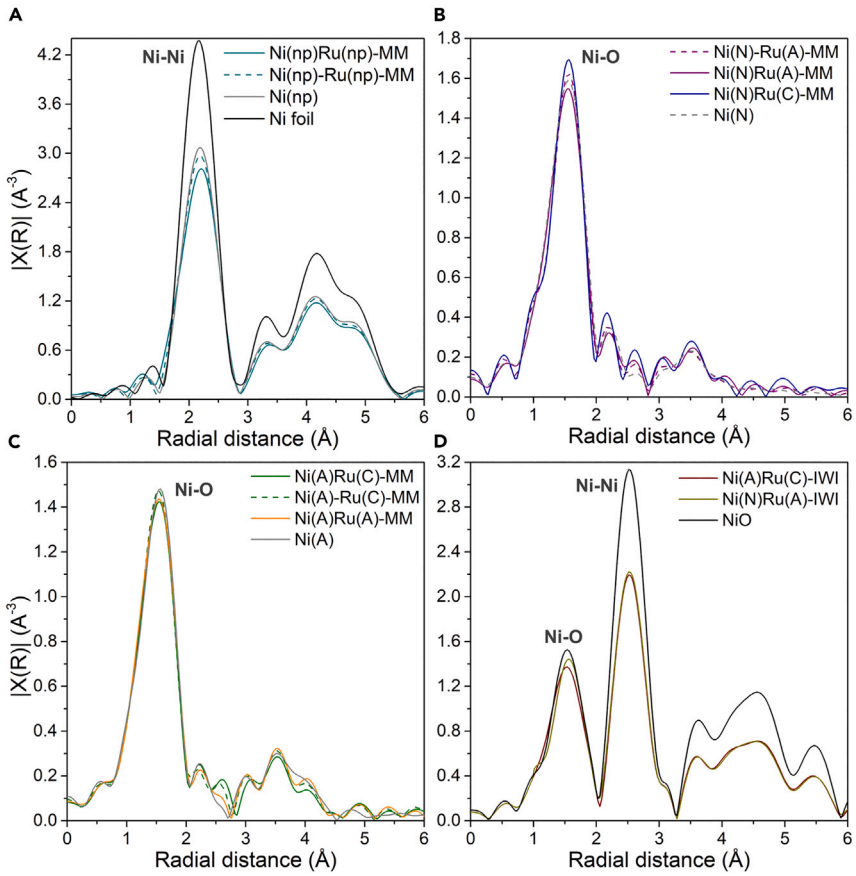

Figure 7. Magnitude of the FT of the EXAFS spectra at the Ni K-edge of the catalysts prepared

(A) Ni nanoparticles, (B) Ni nitrate, and (C) Ni acetate as Ni precursor and (D) prepared by IWI.

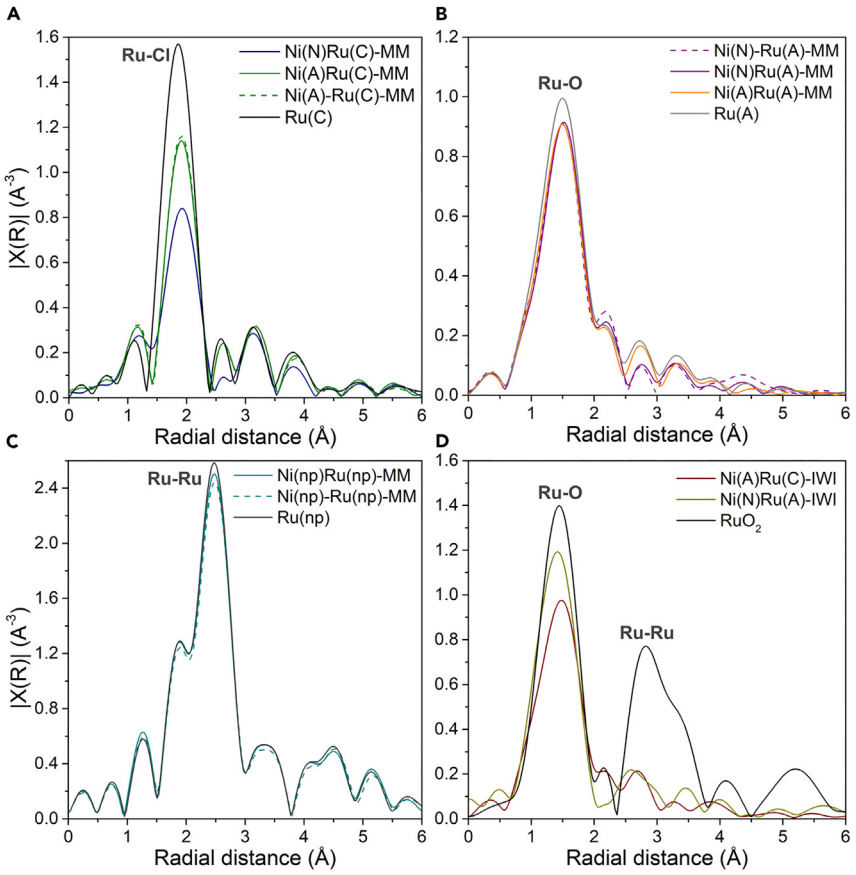

Figure 8. Magnitude of the FT of the EXAFS spectra at the Ru K-edge of the catalysts prepared
(A) Ru chloride, (B) Ru acetate, and (C) Ru nanoparticles as Ru precursor and (D) prepared by IWI.

(V_0, V′, U_0, and U′), using peak positions and FWHM as reported in the literature.[63] "U" and "V" denote the $3d_{3/2}$ and $3d_{5/2}$ spin-orbit components, respectively. Deconvolution of the nickel 2p spectra was conducted by cross-referencing peak positions and FWHM reported in the literature.[64–67] Nickel 2p spectra were deconvoluted using two peaks and two satellites for Ni_2O_3 (two doublets), four peaks and four satellites for NiO (four doublets), two peaks and four satellites for nickel acetate (three doublets), two peaks and two satellites for nickel nitrate (two doublets), and two peaks and two satellites for Ni^0 (two doublets). The deconvolution of the ruthenium 3d spectra followed methodologies described in the literature.[68–71] For the deconvolution of Ru 3d spectra four peaks were used for RuO_2 (two doublets), two peaks for $RuCl_3$ (one doublet), two peaks for $Ru(OH)_3$ (one doublet), two peaks for ruthenium acetate (one doublet), and two peaks for Ru^0 (one doublet). The obtained results are shown in Figure 9, whereas the surface atomic ratios are shown in Table 3. The spectra are normalized with respect to the U‴ peak of ceria and to the adventitious carbon peak in the case of Ru 3d spectra. From the Ce 3d spectra deconvolution, the presence on the surface of all the catalysts of both CeO_2 (Ce^{4+}) and, to a lesser extent, Ce_2O_3 (Ce^{3+}) was identified, consistent with XANES results. The relative proportion of the two oxidation states is shown in Table 1. The surface Ce^{3+} percentage is smaller compared to the bulk, displaying diverse trends among the catalysts prepared using IWI and MM methods. Generally, IWI-prepared catalysts exhibited a higher surface percentage of Ce^{3+} compared to the catalyst prepared using the same precursors with MM, probably due to the formation of Ni-Ce-O and/or Ru-Ce-O bond, as identified from Raman spectra, resulting in higher oxygen defect concentrations.[72] Similar trends were observed in the deconvoluted O 1s spectra (Figure 10), where the peak around 531 eV is usually attributed to oxygen species weakly absorbed on the ceria surface associated with Ce^{3+} ions (O_s), whereas the peaks around 529 eV and 527 eV are attributed to ceria lattice oxygen (O_L).[73–77] The spectra are normalized to the O_L peak. The absorption of oxygen on the IWI-prepared catalyst surfaces was higher compared to the MM counterparts (Table 1), and the two catalysts prepared with Ni nitrate and Ru acetate with MM (Ni(N)Ru(A)-MM and Ni(N)-Ru(A)-MM) presented very similar values. IWI-prepared catalysts showed oxidized forms of Ni_2O_3, NiO, and RuO_2 on their surfaces, and in the case of Ru 3d spectra, metallic Ru presence is an indication of precursor decomposition during calcination at 450°C,[21] demonstrating the complete oxidation (or partial decomposition) of the precursors used. Conversely, MM-prepared catalysts exhibited precursor forms together with oxidized forms of nickel and ruthenium, confirming XAS results of partial precursor oxidation through the milling process. Furthermore, an IWI-prepared catalyst analyzed before calcination (Ni(A)Ru(C)-preIWI) revealed the presence of precursors (Ni acetate and $RuCl_3$), along with NiO, and $Ru(OH)_3$ on its surface, indicating the initial precursor oxidation. Table 2

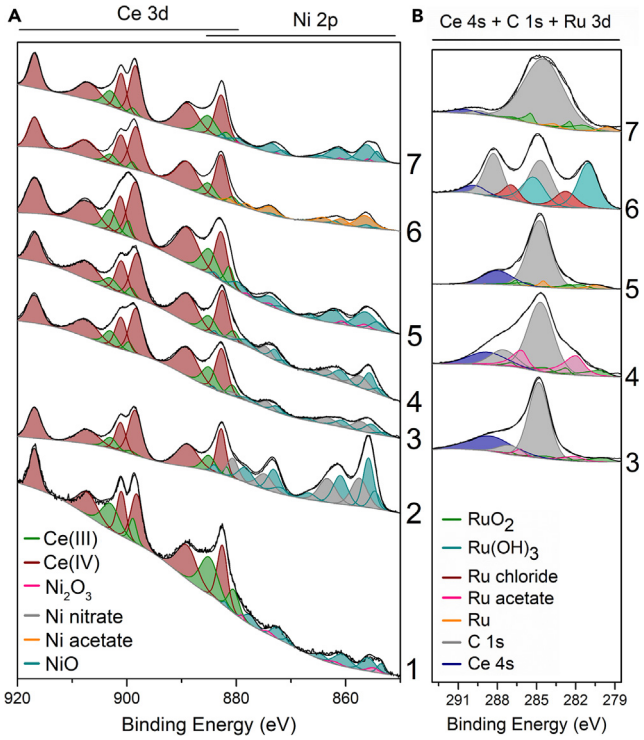

Figure 9. XP spectra of Ce 3d, Ni 2p, and Ru 3d

XP spectra of Ce 3d and Ni 2p (A) and Ru 3d (B) of (1) Ni(N)-IWI, (2) Ni(N)-MM, (3) Ni(N)Ru(A)-MM, (4) Ni(N)-Ru(A)-MM, (5) Ni(N)Ru(A)-IWI, (6) Ni(A)Ru(C)-preIWI, and (7) Ni(A)Ru(C)-IWI. The C 1s peak at 284.8 eV corresponds to adventitious carbon, whereas the peak at around 289.0 eV is related to C in the O-C=O form (acetate).

displays the percentage of NiO and RuO_2 identified on the surface in relation to total Ni and Ru amounts, respectively. For IWI-prepared catalysts, oxidation appeared gradient-like within the particle: the surface oxidation was more advanced than in the bulk. Conversely, in MM-prepared catalysts, the surface oxidation varied based on the metal type; for Ni, surface forms were more oxidized compared to the bulk, whereas for Ru, precursor amounts on the surface were higher than in the bulk. The Ni/Ru surface ratio was higher in IWI-calcined catalysts compared to MM counterparts, whereas the IWI catalyst analyzed before its calcination presents a value similar to MM catalysts.

Table 3. Surface atomic ratios and binding energies of Ni (2p3/2) and Ru (Ru 3d5/2) main peak of each form detected in the catalysts

Sample	*Ni/Ru*	*(Ni+Ru)/Ce or Ni/Ce*	*Ni forms and main peaks BE (eV)*	*Ru forms and main peaks BE (eV)*
Ni(N)-IWI	–	0.48	Ni_2O_3 (855.0) NiO (853.5, 855.9)	–
Ni(N)-MM	–	2.65	Ni nitrate (857.5) NiO (854.7, 855.9)	–
Ni(N)Ru(A)-MM	1.1	1.11	Ni nitrate (857.2) NiO (853.1, 855.3)	Ru acetate (282.1) RuO_2 (279.7)
Ni(N)-Ru(A)-MM	0.7	2.00	Ni nitrate (857.3) NiO (854.0, 855.6)	Ru acetate (282.0) RuO_2 (280.0)
Ni(N)Ru(A)-IWI	4.2	0.75	Ni_2O_3 (856.5) NiO (854.2, 856.4)	RuO_2 (281.5) Ru (280.3)
Ni(A)Ru(C)-preIWI	1.6	0.84	Ni acetate (856.5) NiO (854.7, 856.2)	$RuCl_3$ (282.7) $Ru(OH)_3$ (281.0)
Ni(A)Ru(C)-IWI	8.6	0.72	Ni_2O_3 (855.9) NiO (854.3, 856.2)	RuO_2 (281.2) Ru (279.5)

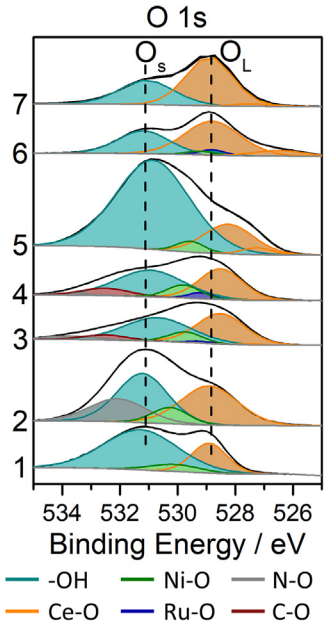

Figure 10. XP spectra of O 1s of (1) Ni(N)-IWI, (2) Ni(N)-MM, (3) Ni(N)Ru(A)-MM, (4) Ni(N)-Ru(A)-MM, (5) Ni(N)Ru(A)-IWI, (6) Ni(A)Ru(C)-preIWI, and (7) Ni(A)Ru(C)-IWI. O_s indicates the peak related to oxygen species weakly absorbed on the ceria surface, whereas O_L indicates the peak related to ceria lattice oxygen

The atomic ratio between the two metals Ni and Ru with respect to Ce can be used as an indicator of metal dispersion on the support surface, which was higher in MM-prepared catalysts.

Reducibility of the catalysts

The reducibility of selected catalysts was analyzed through H_2-TPR (Ni(N)-Ru(A)-MM, Ni(N)Ru(A)-IWI, and Ni(A)Ru(C)-IWI). The results have been reported in Figure 11. All profiles presented two peaks at high temperatures related to the ceria support: the one at around 732°C–778°C corresponds to the reduction of bulk Ce(IV) to Ce(III) and that close to 400°C is ascribed to the surface reduction of ceria involving bridging OH group formation.[78] In the case of the Ni(A)Ru(C)-IWI catalyst, a band with a maximum at 608°C is also visible, attributed to the reduction of the Ni-*O*-Ce entities.[79] The Ni(N)Ru(A)-IWI sample exhibited a prominent peak at 300°C, assigned to the reduction of NiO species present on the surface.[80] Additionally, this profile displayed two peaks at lower temperatures, attributed to the reduction of Ru, at 85°C and 130°C. The presence of multiple peaks suggests the coexistence in this sample of RuO_x in a well-dispersed state and well-crystallized RuO_2 species, with the latter being more difficult to reduce.[81] The other catalysts presented a single peak at around 100°C, assigned to the simultaneous reduction of Ni and Ru species. The presence of only one low-temperature peak associated with the reduction of both

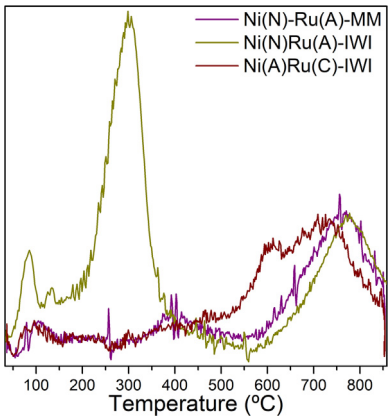

Figure 11. H_2-TPR profiles of Ni(N)Ru(A)-IWI, Ni(N)-Ru(A)-MM, and Ni(A)Ru(C)-IWI

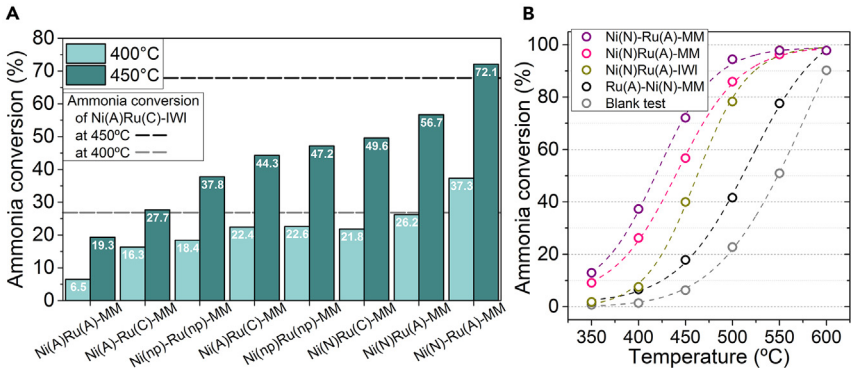

Figure 12. Variable-temperature ammonia conversion

(A) catalysts prepared using the MM method and different precursors and (B) catalysts prepared with nickel nitrate and ruthenium acetate using different methods. The blank test was performed using the same volume of SiC without catalyst. Reaction test conditions: GHSV of 3660 h^{-1}, 0.1 g of catalyst, F/W of 15.0 L h^{-1} g^{-1}, Ar:NH_3 = 1.2:1 M, 1 bar.

metals indicates a strong interaction between them in the prepared bimetallic samples,[82] which can explain the superior catalytic performance of these two samples compared to the other catalysts tested.

Ammonia decomposition performance

The catalysts were tested for the decomposition of ammonia reaction between 350°C and 600ºC. The ammonia conversion results are shown in Figure 12. The catalyst prepared using nickel and ruthenium acetates demonstrated the lowest activity (6.5% and 19.3% at 400°C and 450°C, respectively, Figure 12A), whereas the catalyst prepared under the exact same conditions of milling (15 Hz, 10 min, B/P = 8.5) using nickel nitrate and ruthenium acetate presented an ammonia conversion of 26.2% at 400°C and 56.7% at 450°C. These findings underscore the key role of precursor types, particularly highlighting the influence of the interactions among the three precursors (including cerium oxide), since the same precursor showed results that vary with the second metal precursor, as in the example above. Notably, the two-step catalyst preparation (10 min with the Ni and ceria precursor followed by 10 min after adding the Ru precursor) revealed enhanced catalyst activity in specific precursor combinations, as in the case of the catalyst prepared using Ni nitrate and Ru acetate, which is the one that showed the highest activity. If prepared in two steps, this catalyst allows to increase the conversion of ammonia by 11.1% and 15.4% respectively, at 400°C and 450°C. However, altering the precursor order—incorporating the support and Ru acetate in the first step (10 min) and adding Ni nitrate in a subsequent 10-min step—resulted in a significant decrease in conversion (Figure 12B). This may be related to the residence time of the precursors in the synthesis system. Furthermore, by comparing the results obtained with those of the catalyst prepared by IWI method using the same precursors, a higher activity was determined in the case of the catalysts prepared with MM (Figure 12B). The comparison of the ammonia conversion levels obtained with the catalyst prepared by IWI using Ni acetate and Ru chloride reported in our previous works[21] (Figure 12A) revealed higher conversion rate in the case of the catalyst prepared via MM prepared in two steps using Ni nitrate and Ru acetate.

The catalyst prepared with MM that presented the highest catalytic activity was tested in a long-term reaction (100 h) at 450°C. The result obtained for the conversion of ammonia is shown in Figure 13. The catalyst presented an initial deactivation, where the conversion decreased

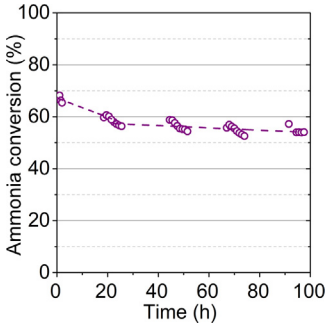

Figure 13. Stability test in the decomposition of ammonia at 450°C

Reaction test conditions: GHSV of 3660 h^{-1}, 0.1 g of catalyst, F/W of 15.0 L h^{-1} g^{-1}, Ar:NH_3 = 1.2:1 M, 1 bar.

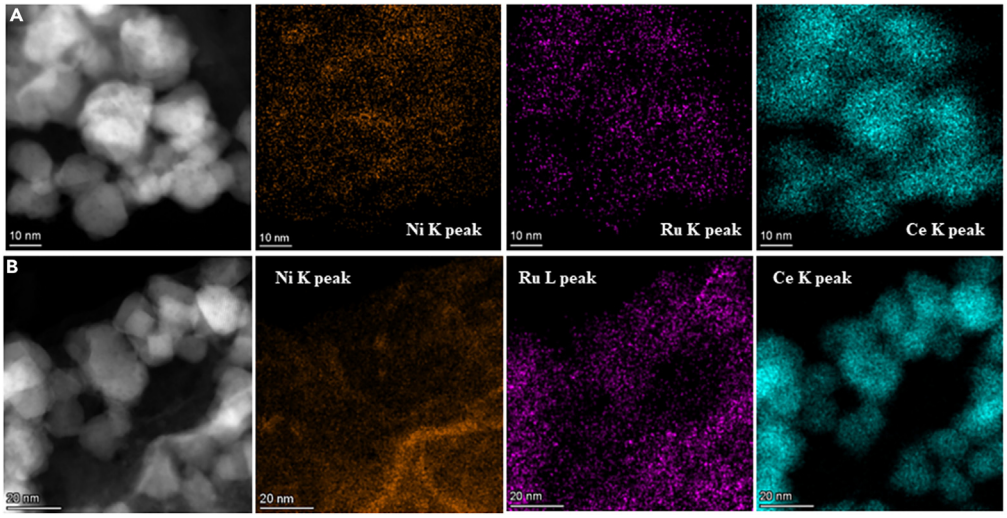

Figure 14. EDX maps of Ni(N)-Ru(A) catalysts
(A) Ni(N)-Ru(A)-IWI and (B) Ni(N)-Ru(A)-MM (using Ni, Ru, and Ce K-peaks).

from 67% to 61%, and after around 20 h of reaction, the catalyst was stable over the subsequent 80 h of reaction at an average conversion of 56%.

Post-reaction characterization

Ni(N)-Ru(A)-MM and Ni(N)Ru(A)-IWI samples have been analyzed using HRTEM/STEM and XPS after being tested in ammonia decomposition reaction up to 600°C. From HRTEM images, the average size of the ceria particles has been estimated: 19 nm for MM-prepared catalysts and 22 nm for IWI-prepared one. Compared to pre-reaction sizes (Figure 1), there was an increase of around 6 nm for the MM-prepared catalyst ceria particles, and around 5 nm for the IWI-prepared catalyst, attributed to their partial sintering at elevated temperatures. The distribution of Ni and Ru particles remained uniform on the surface, as evidenced by EDX mapping (Figure 14).

In Figure 15, the XPS spectra of the same samples post-reaction are reported. The spectra presented oxidized forms of both metals, NiO and RuO_2, and, to a lesser extent, metallic Ni [2.7 and 0.7% of the total for Ni(N)-Ru(A)-MM and Ni(N)Ru(A)-IWI, respectively] and Ru (34.2 and 33.8%) were also identified. The analysis of the amount of Ce^{3+} compared to total Ce showed an increase in reduced ceria for both catalysts after the reaction, particularly notable for the MM-catalyst, with values of 27.0% and 23.1% for the MM- and IWI-prepared catalysts, respectively, compared to their initial states (Table 1). The surface dispersion of Ru and Ni slightly decreased for the MM-prepared catalyst to a value of 1.28, while remaining around 0.69 for the IWI catalyst, suggesting partial sintering of metal particles on the MM-prepared catalyst's surface, probably due to the absence of the calcination step during its synthesis, unlike the IWI-prepared catalyst. The Ni to Ru ratio increased to 2.6 for the MM-prepared catalyst, whereas it stayed at 4.2 for the IWI-prepared catalyst (compared to the values in Table 3 for the catalysts as prepared).

DISCUSSION

Understanding the relationship among the catalyst properties and activity

HRTEM analysis revealed initial morphology and size differences between the catalysts prepared by the two methods, mainly due to the calcination step of the catalyst prepared by IWI, which led to the complete oxidation of the precursors, as confirmed by XPS, XAS, and XRD results. Both IWI and MM catalysts showed crystallites associated with ceria and Ni and Ru forms; however, distinguishing their individual particles was difficult, indicating an intimate contact between the two active metals and with the support. The size of the metal particles was estimated through the crystallite size obtained with XRD. NiO particles in IWI-prepared catalysts measured approximately 9 nm, whereas the catalysts prepared via MM using nickel nitrate, those that showed the highest catalytic activity, did not exhibit peaks related to Ni species, suggesting their extremely small size and high dispersion. Catalysts prepared with Ni acetate displayed larger particles, ranging between 50 and 72 nm (Table 2) and those prepared using Ni nanoparticles presented supported Ni metallic particles of about 50 nm. It was not possible to determine the average crystallite dimensions of ruthenium species in the catalysts, due to its low content (1 wt.%). Notably, ammonia conversion with MM catalysts increased proportionally with decreasing the nickel particle size. The catalytic activity of the IWI-prepared catalysts also exhibited significant dependency on the precursors used, since the catalyst prepared using Ni nitrate and Ru acetate demonstrated a conversion of 40% at 450°C, whereas Ni(A)Ru(C)-IWI achieved 68.2% at the same temperature. Although no specific differences related to Ni or Ru particle size were identified in these two catalysts, distinct interactions of these metals with the ceria support were observed. In particular, the catalyst that exhibited the highest activity showed the largest amount of reduced ceria (Table 1). This trend was consistent across all catalysts,

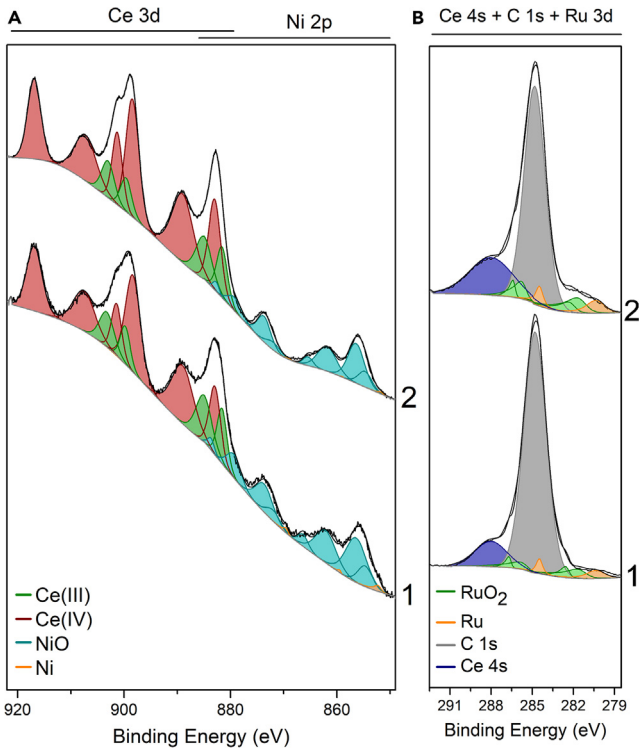

Figure 15. XP spectra of Ce 3d and Ni 2p (A) and Ru 3d (B) of the catalysts (1) Ni(N)-Ru(A)-MM and (2) Ni(N)Ru(A)-IWI post-reaction. The C 1s peak at 284.8 eV corresponds to adventitious carbon

showing a progressive increase in conversion with the increase of reduced ceria (Figure 12). This can be attributed to a relationship between oxygen vacancies and Ce^{3+} presence, as well as enhanced electron transfer capacity.[83] The increase in the reduced form of ceria also correlates well with the increase in the intensity of the band related to defects in the structure of ceria of the Raman spectra. It has been reported in the literature that the interaction between oxygen vacancies in the support and the active phase facilitates the recombinative desorption of N atoms, achieving higher catalytic performance in the decomposition of NH_3, due to the increase in electron density that could be transferred from the basic sites of the support at the surface of the active phase.[84,85] The XPS analysis of the surface composition of some of the prepared catalysts revealed that the presence of reduced surface ceria shows minimal differences between the IWI- and MM-prepared bimetallic catalysts, although the former exhibited a slightly higher Ce^{3+} content. Moreover, there were no substantial distinctions found among catalysts prepared using identical precursors (Ni nitrate and Ru acetate) but differing in one or two milling steps. Figure 16 shows the relationship between the conversion, the amount of bulk Ce^{3+}, and the relationship between the D and F_{2g} areas. The strong interaction between the metal precursors and the support is further supported by the results obtained with XANES and EXAFS, where the partial

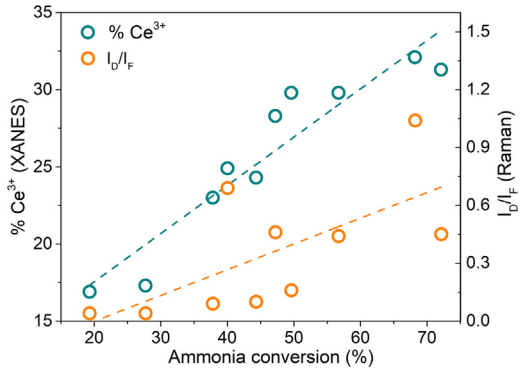

Figure 16. Relationship between the ammonia conversion, the amount of Ce^{3+} (XANES), and the relationship between the D and F_{2g} areas (Raman spectroscopy)

oxidation of the metals due to the milling process was determined (Table 2), confirmed by XPS analysis. By quantifying the oxidized form of the two metals, considerations can be made regarding the intensity of interaction among the three precursors in the catalysts prepared via MM, given that the milling conditions employed are identical. Catalysts demonstrating a higher presence of Ni- and Ru-oxidized forms in the bulk exhibited increased ammonia conversion, particularly those prepared using nickel nitrate as a precursor. Notably, the catalyst showing the highest activity (Ni(N)-Ru(A)-MM) presented the highest presence of bulk RuO_2, followed by the same catalyst prepared with the same precursors but in a single milling step. This suggests that although the size of the nickel particles is influential in tuning the catalyst activity, the interaction between ruthenium and the other precursors is equally crucial. Regarding the surface composition, analyzed with XPS, these two catalysts exhibited distinct behaviors: the catalyst prepared in two milling steps shows a higher quantity of Ni-oxidized forms on the surface compared to the bulk, whereas for ruthenium, the opposite trend is observed. This indicates the presence of oxidation gradients within the catalyst particles. Upon analyzing the surface atomic ratios among the identified elements of the catalysts, it was possible to conclude that MM-prepared catalysts exhibit a notably higher metal dispersion on the surface compared to those prepared by IWI (1–2 vs. 0.8 in the case of bimetallic catalysts, respectively), thereby increasing the number of available active sites. Additionally, MM-prepared catalysts show a higher presence of Ru, as evidenced by the diminishing Ni/Ru ratio, dropping from 4.2–8.6 (IWI catalysts) to 0.7 in the catalyst displaying the highest catalytic activity. Comparing the catalysts prepared using Ni nitrate and Ru acetate in one or two milling steps, it can be observed that the catalyst prepared in two steps displayed the greatest presence of Ru on the surface, even surpassing that of Ni, and a higher dispersion. As regards the preparation of the catalyst by milling in two steps, depending on the type of precursors it has been demonstrated that different results are achieved: in the case of Ni(A)-Ru(C)-MM and Ni(np)-Ru(np)-MM the catalyst activity decreased, whereas in the case of Ni(N)-Ru(A)-MM it increased, indicating that the increase in milling time of the Ni precursor with ceria, from 10 to 20 min, has different effects depending on the precursor used. In general, catalysts prepared in one step presented different characteristics compared to those prepared in two steps, underlining the possibility of tuning the catalytic activity by varying the milling conditions.

The analysis of the catalyst reducibility revealed interesting differences, particularly between the two catalysts synthesized using IWI. In the catalyst prepared using Ni nitrate and Ru acetate as precursors, which exhibited the lowest activity among the two, the reduction of Ru and Ni species occurs at different temperatures, whereas in the catalyst prepared with Ni acetate and Ru chloride, which showed higher activity, the reduction of Ni and Ru species occurred simultaneously and at lower temperatures. The MM-catalyst with the highest activity among those prepared showed an H_2-TPR profile closely similar to that of Ni(A)Ru(C)-IWI. This similarity further underscores the importance of the interaction between Ni and Ru in influencing catalytic activity: higher interaction corresponds to increased activity. Prior to the reaction, the catalysts are reduced at 300°C with H_2, which means that in the case of the most active catalysts, at this temperature both the Ni and Ru species are already completely reduced. The characterization of the catalysts employed in the reaction revealed slight sintering of ceria particles, similar for both synthesis methods. Additionally, the surface dispersion of Ru and Ni slightly decreased in the MM-prepared catalyst. The estimation of the surface atomic ratio between Ni and Ru showed an increase in the surface Ni amount in the MM-prepared catalyst compared to Ru, suggesting the sintering of Ru particles. The IWI-prepared catalyst exhibited higher stability than its MM-prepared counterpart, also during the stability test, where the catalyst exhibited an initial deactivation, followed by a phase of constant activity. This enhanced stability is likely attributed to the calcination step used in the preparation of the IWI catalyst. Comparing the hydrogen production achieved at 450°C in the stable phase of the catalyst prepared by MM (305.8 $mmol_{H2}\ g_{cat}^{-1}\ h^{-1}$) with results obtained in the literature under similar or more favorable reaction conditions (WHSV of 136000 $mL_{NH3}\ g_{met}^{-1}\ h^{-1}$ or lower), the prepared catalyst demonstrates superior activity compared to nickel-based catalysts, such as Ni/MgO (19.1 $mmol_{H2}\ g^{-1}\ h^{-1}$),[5] or promoted Ni catalyst, such as 2wt.%K-15wt.%Ni/Al_2O_3 (20.5 $mmol_{H2}\ g^{-1}\ h^{-1}$),[86] and bimetallic configurations like Ni-Co supported on Y_2O_3 (168.6 $mmol_{H2}\ g^{-1}\ h^{-1}$ at 500°C).[87] However, the MM-catalyst exhibits lower activity compared to catalysts containing ruthenium.[88]

Conclusions

Mechanochemical milling synthesis of $NiRu/CeO_2$ catalysts demonstrated the ability to achieve better ammonia conversion for hydrogen production compared to catalysts prepared by the conventional incipient wetness impregnation method. The use of different types of metal precursors enabled significant modulation of catalyst activity. Moreover, catalysts prepared by ball milling in two steps, milling first the Ni precursor with the ceria support and then the Ru precursor in a second step, performed better than catalysts prepared in a single step by milling together the Ni and Ru precursors with the ceria support. Specifically, catalysts with smaller Ni particle size and with a strong interaction between the metals and cerium oxide proved to be the main characteristics enhancing the catalytic activity in the decomposition of ammonia. In particular, the mechanochemical method employed demonstrated the capacity to change the oxidation state of Ni and Ru, and this capacity strongly depends on the type of precursors used. A specific interaction between the precursors and the support achieved by mechanochemistry allows an increase in oxygen vacancies in the ceria structure, usually related to an increased electron transfer capacity and better catalytic performance.

Limitations of the study

The measurement of the relative hardness of the precursors could provide valuable information regarding the characteristics of the resulting catalysts. Further transmission electron microscopy studies are needed to precisely determine the structural characteristics of the active phase.

STAR★METHODS

Detailed methods are provided in the online version of this paper and include the following:

- KEY RESOURCES TABLE
- RESOURCE AVAILABILITY
  - Lead contact
  - Materials availability
  - Data and code availability
- METHOD DETAILS
  - Preparation of catalysts
  - Catalyst characterization techniques
  - Catalytic tests
- QUANTIFICATION AND STATISTICAL ANALYSIS

ACKNOWLEDGMENTS

This work was funded by MICINN/FEDER PID2021-124572OB-C31 and PID2021-124572OB-C33 and 2021 SGR 01061 projects. J.L. is a Serra Húnter Fellow and is grateful to the ICREA Academia program. ICN2 acknowledges funding from Generalitat de Catalunya 2021SGR00457. This study is part of the Advanced Materials program and was supported by MCIN with funding from the European Union NextGenerationEU (PRTR-C17.I1) and by Generalitat de Catalunya. ICN2 is supported by the Severo Ochoa program from Spanish MCIN/AEI (Grant No.: CEX2021-001214-S) and is funded by the CERCA Program/Generalitat de Catalunya. A.G.M. is grateful to Grant RYC2021-033479-I funded by MCIN/AEI/10.13039/501100011033 and by European Union NextGenerationEU/PRTR.

AUTHOR CONTRIBUTIONS

I.L. was responsible for the preparation and characterization of the catalysts, for the analysis of results and for writing the manuscript. I.S. was responsible for the preparation and reaction test of the catalysts. X.G. was responsible for the characterization. A.G., J.A., X.H., L.P., J.P., E.E.V., and C.M. contributed to the characterization. C.E. and J.L. provided the resources and supervised the project. All the authors reviewed the manuscript.

DECLARATION OF INTERESTS

The authors declare no competing interests.

Received: December 27, 2023
Revised: March 12, 2024
Accepted: May 16, 2024
Published: May 21, 2024

REFERENCES

1. European Commission (2019). Communication from the Commission to the European Parliament, the Council, the European Economic and Social Committee and the Committee of the Regions (The European Green Deal). COM/2019/640 final.
2. European Commission (2020). Communication from the Commission to the European Parliament, the Council, the European Economic and Social Committee and the Committee of the Regions. In A hydrogen strategy for a climate-neutral Europe. COM/2020/301 final.
3. Crabtree, G.W., Dresselhaus, M.S., and Buchanan, M.V. (2004). The Hydrogen Economy. Phys. Today *57*, 39–44. https://doi.org/10.1063/1.1878333.
4. Zamfirescu, C., and Dincer, I. (2009). Ammonia as a green fuel and hydrogen source for vehicular applications. Fuel Process. Technol. *90*, 729–737. https://doi.org/10.1016/j.fuproc.2009.02.004.
5. Ulucan, T.H., Wang, J., Onur, E., Chen, S., Behrens, M., and Weidenthaler, C. (2024). Unveiling the Structure–Property Relationship of MgO-Supported Ni Ammonia Decomposition Catalysts from Bulk to Atomic Structure by In Situ/Operando Studies. ACS Catal. *14*, 2828–2841. https://doi.org/10.1021/acscatal.3c05629.
6. Bao, Z., Li, D., Wu, Y., Jin, L., and Hu, H. (2024). Efficient Ni/Y_2O_3 catalyst prepared by sol-gel self-combustion method for ammonia decomposition to hydrogen. Int. J. Hydrogen Energy *53*, 848–858. https://doi.org/10.1016/j.ijhydene.2023.11.293.
7. Li, S., Liu, X., Guo, Y., and Wang, Y. (2024). Highly active and stable Ni@SiO_2 catalyst for ammonia decomposition. Fuel *368*, 131543. https://doi.org/10.1016/j.fuel.2024.131543.
8. Wang, Z., Luo, H., Wang, L., Li, T., Li, S., and Liu, Y.Q. (2024). Promotion of Low-Temperature Catalytic Activity of Ru-Based Catalysts for Ammonia Decomposition via Lanthanum and Cesium Codoping. ACS Sustain. Chem. Eng. *12*, 5620–5631. https://doi.org/10.1021/acssuschemeng.4c00176.
9. Yang, J., Zhao, X., Qi, X., Wen, J., and Zhang, H. (2024). Potassium-promoted Ru-MCM-41 catalyst via in situ loading for effective low-temperature ammonia decomposition. New J. Chem. *48*, 8195–8202. https://doi.org/10.1039/D3NJ05953G.
10. Guo, X.Y., Wang, J.H., Zhang, Q., Li, T.Z., Dong, H., Jia, C.J., Li, C., and Zhang, Y.W. (2024). Alkaline earth metal promoted hydrogen production from ammonia decomposition over Ni/La_2O_3-based catalysts. Appl. Catal., B *348*, 123844. https://doi.org/10.1016/j.apcatb.2024.123844.
11. Teng, Q., Sang, J., Chen, G., Tao, H., Wang, Y., Li, H., Guan, W., Ding, C., Liu, F., and Zhu, L. (2024). Ru/Attapulgite as an Efficient and Low-Cost Ammonia Decomposition Catalyst. Catalysts *14*, 197. https://doi.org/10.3390/catal14030197.
12. Ju, X., Liu, L., He, T., and Chen, P. (2024). Tuning the Interaction Between Ru Nanoparticles and Nd_2O_3 to Enhance Hydrogen Formation from Ammonia Decomposition. Top. Catal. https://doi.org/10.1007/s11244-024-01926-8.
13. Winter, F.L., Diehl, P., Telaar, P., Watermann, C.M., Kaluza, S., Muhler, M., Apfel, U.P., and Zeidler-Fandrich, B. (2024). Influence of the

catalyst precursor for cobalt on activated carbon applied in ammonia decomposition. Catal. Today *429*, 114502. https://doi.org/10.1016/j.cattod.2023.114502.

14. Hu, H., Tu, Z., Yan, X., Chen, X., Zhou, L., Lu, Z.H., Ye, R., Feng, G., and Zhang, R. (2024). Effects of Organic Compounds on Ni/AlLaCe Catalysts for Ammonia Decomposition to Hydrogen. Ind. Eng. Chem. Res. *63*, 3910–3920. https://doi.org/10.1021/acs.iecr.3c04390.
15. Shin, J., Jung, U., Kim, J., Kim, K.D., Song, D., Park, Y., An, B.S., and Koo, K.Y. (2024). Elucidating the effect of Ce with abundant surface oxygen vacancies on $MgAl_2O_4$-supported Ru-based catalysts for ammonia decomposition. Appl. Catal. B *340*, 123234. https://doi.org/10.1016/j.apcatb.2023.123234.
16. Yu, X., Yin, F., Li, G., Zhang, J., and Chen, B. (2024). Preparation of nickel aluminate supported Ni nanocatalyst and its catalytic activity for ammonia decomposition to produce hydrogen. Int. J. Hydrogen Energy. https://doi.org/10.1016/j.ijhydene.2024.04.019.
17. Kim, E.-J., Woo Kim, Y., Cho, Y., Kweon, S., Bum Park, M., Shin, C.-H., Min, H.-K., and An, K. (2024). Metallic nickel exsolved from a two-dimensional MWW-type zeolitic nickel silicate: An effective catalyst for ammonia decomposition. Chem. Eng. J. *485*, 149871. https://doi.org/10.1016/j.cej.2024.149871.
18. Chen, T.B., Rabiee, H., Yan, P., Zhu, Z., and Ge, L. (2024). Enhancing the Ammonia Catalytic Decomposition of Lanthanum Strontium Titanate Nickel Perovskite Catalysts via a Balanced Cation Doping and Deficiency Strategy. Energy Fuels *38*, 5449–5456. https://doi.org/10.1021/acs.energyfuels.4c00345.
19. Hund, S., Gómez-Cápiro, O., Ruland, H., Heppke, E.M., and Lerch, M. (2024). Ni_2Mo_3N: crystal structure, thermal properties, and catalytic activity for ammonia decomposition. Z. Naturforsch. *79*, 147–153. https://doi.org/10.1515/znb-2023-0071.
20. Du, M., Guo, L., Ren, H., Tao, X., Li, Y., Nan, B., Si, R., Chen, C., and Li, L. (2023). Non-Noble $FeCrO_x$ Bimetallic Nanoparticles for Efficient NH_3 Decomposition. Nanomaterials *13*, 1280. https://doi.org/10.3390/nano13071280.
21. Lucentini, I., Colli, G.G., Luzi, C.D., Serrano, I., Martínez, O.M., and Llorca, J. (2021). Catalytic ammonia decomposition over Ni-Ru supported on CeO_2 for hydrogen production: Effect of metal loading and kinetic analysis. Appl. Catal., B *286*, 1–10. https://doi.org/10.1016/j.apcatb.2021.119896.
22. Lucentini, I., Casanovas, A., and Llorca, J. (2019). Catalytic ammonia decomposition for hydrogen production on Ni, Ru and Ni–Ru supported on CeO_2. Int. J. Hydrogen Energy *44*, 12693–12707. https://doi.org/10.1016/j.ijhydene.2019.01.154.
23. Lucentini, I., Garcia, X., Vendrell, X., and Llorca, J. (2021). Review of the Decomposition of Ammonia to Generate Hydrogen. Ind. Eng. Chem. Res. *60*, 18560–18611. https://doi.org/10.1021/acs.iecr.1c00843.
24. Amrute, A.P., De Bellis, J., Felderhoff, M., and Schüth, F. (2021). Mechanochemical Synthesis of Catalytic Materials. Chem. Eur J. *27*, 6819–6847. https://doi.org/10.1002/chem.202004583.
25. Rojas-Chávez, H., Cruz-Martínez, H., Flores-Rojas, E., Juárez-García, J.M., González-Domínguez, J.L., Daneu, N., and Santoyo-Salazar, J. (2018). The mechanochemical synthesis of PbTe nanostructures: Following the Ostwald ripening effect during milling. Phys. Chem. Chem. Phys. *20*, 27082–27092. https://doi.org/10.1039/c8cp04915g.
26. Li, X., Wen, X., Zhao, H., Ma, Z., Yu, L., Li, C., Liu, C., Guo, Q., and Liu, Y. (2019). The formation and evolution mechanism of amorphous layer surrounding Nb nano-grains in Nb-Al system during mechanical alloying process. J. Alloys Compd. *779*, 175–182. https://doi.org/10.1016/j.jallcom.2018.11.135.
27. Danielis, M., Colussi, S., De Leitenburg, C., Soler, L., Llorca, J., and Trovarelli, A. (2019). The effect of milling parameters on the mechanochemical synthesis of Pd-CeO_2 methane oxidation catalysts. Catal. Sci. Technol. *9*, 4232–4238. https://doi.org/10.1039/c9cy01098j.
28. Danielis, M., Divins, N.J., Llorca, J., Soler, L., Garcia, X., Serrano, I., Betancourt, L.E., Xu, W., Rodríguez, J.A., Senanayake, S.D., et al. (2023). In situ investigation of the mechanochemically promoted Pd–Ce interaction under stoichiometric methane oxidation conditions. EES Catal. *1*, 144–152. https://doi.org/10.1039/d2ey00067a.
29. Divins, N.J., Braga, A., Vendrell, X., Serrano, I., Garcia, X., Soler, L., Lucentini, I., Danielis, M., Mussio, A., Colussi, S., et al. (2022). Investigation of the evolution of Pd-Pt supported on ceria for dry and wet methane oxidation. Nat. Commun. *13*, 5080. https://doi.org/10.1038/s41467-022-32765-4.
30. Fazlikeshteli, S., Vendrell, X., and Llorca, J. (2023). Low-temperature partial oxidation of methane over Pd–Ni bimetallic catalysts supported on CeO_2. Int. J. Hydrogen Energy *48*, 12024–12035. https://doi.org/10.1016/j.ijhydene.2022.07.020.
31. Koch, C.C. (1990). Amorphization by mechanical alloying. J. Non-Cryst. Solids *117–118*, 670–678. https://doi.org/10.1016/0022-3093(90)90620-2.
32. Zhang, Z.W., Zhou, J.E., Xi, S.Q., Ran, G., Li, P.L., and Zhang, W.X. (2004). Formation of crystalline and amorphous solid solutions of W-Ni-Fe powder during mechanical alloying. J. Alloys Compd. *370*, 186–191. https://doi.org/10.1016/j.jallcom.2003.09.012.
33. Wang, H., Gordon, R.G., Alvis, R., and Ulfig, R.M. (2009). Atomic layer deposition of ruthenium thin films from an amidinate precursor. Chem. Vap. Depos. *15*, 312–319. https://doi.org/10.1002/cvde.200906789.
34. Qiao, H., Wei, Z., Yang, H., Zhu, L., and Yan, X. (2009). Preparation and characterization of NiO nanoparticles by anodic arc plasma method. J. Nanomater. *2009*, 1–5. https://doi.org/10.1155/2009/795928.
35. Syed-Hassan, S.S.A., and Nor-Azemi, S.N.I. (2016). Gasification of nickel-preloaded oil palm biomass with air. Bull. Chem. React. Eng. Catal. *11*, 262–272. https://doi.org/10.9767/bcrec.11.3.566.262-272.
36. Derevyannikova, E.A., Kardash, T.Y., Kibis, L.S., Slavinskaya, E.M., Svetlichnyi, V.A., Stonkus, O.A., Ivanova, A.S., and Boronin, A.I. (2017). The structure and catalytic properties of Rh-doped CeO_2 catalysts. Phys. Chem. Chem. Phys. *19*, 31883–31897. https://doi.org/10.1039/c7cp06573f.
37. Kurnatowska, M., Kepinski, L., and Mista, W. (2012). Structure evolution of nanocrystalline $Ce_{1-x}Pd_xO_{2-y}$ mixed oxide in oxidizing and reducing atmosphere: Reduction-induced activity in low-temperature CO oxidation. Appl. Catal. B *117–118*, 135–147. https://doi.org/10.1016/j.apcatb.2011.12.034.
38. Sartoretti, E., Novara, C., Giorgis, F., Piumetti, M., Bensaid, S., Russo, N., and Fino, D. (2019). In situ Raman analyses of the soot oxidation reaction over nanostructured ceria-based catalysts. Sci. Rep. *9*, 3875. https://doi.org/10.1038/s41598-019-39105-5.
39. Bickley, R.I., Edwards, H., Rose, S.J., and Gustar, R. (1990). A Raman spectroscopic study of nickel(II) acetate, $Ni(CH_3COO)_2$ and its aqueous and methanolic solutions. J. Mol. Struct. *238*, 15–26. https://doi.org/10.1016/0022-2860(90)85002-Z.
40. Gu, Y., Jiang, X., Sun, W., Bai, S., Dai, Q., and Wang, X. (2018). $_{1,2}$-Dichloroethane Deep Oxidation over Bifunctional Ru/Ce_xAl_y Catalysts. ACS Omega *3*, 8460–8470. https://doi.org/10.1021/acsomega.8b00592.
41. Qualcomm, M.G. (2020). Synthesis and characterization of layered transition metal trihalides MCl3 (M = Ru, Mo, Ti, Cr) and CrX3 (X = Cl, Br, I) (Brandenburgischen Technischen Universität). PhD dissertation. https://doi.org/10.26127/BTUOpen-5282.
42. Sandilands, L.J., Tian, Y., Plumb, K.W., Kim, Y.-J., and Burch, K.S. (2015). Scattering Continuum and Possible Fractionalized Excitations in α-$RuCl_3$. Phys. Rev. Lett. *114*, 147201–147205. https://doi.org/10.48550/arXiv.1504.05202.
43. Yang, W., Liu, H., Li, Y., and He, D. (2016). Interaction mechanism of $Ni(NO_3)_2{\cdot}6H_2O$ and P123 in preparing highly-dispersed Ni/SBA-15 catalytic materials. Microporous Mesoporous Mater. *228*, 174–181. https://doi.org/10.1016/j.micromeso.2016.03.044.
44. Vivek, S., Arunkumar, P., and Babu, K.S. (2016). In situ generated nickel on cerium oxide nanoparticle for efficient catalytic reduction of 4-nitrophenol. RSC Adv. *6*, 45947–45956. https://doi.org/10.1039/c6ra04120e.
45. Lawson, K., Wallbridge, S.P., Catling, A.E., Kirk, C.A., and Dann, S.E. (2023). Determination of layered nickel hydroxide phases in materials disordered by stacking faults and interstratification. J. Mater. Chem. A Mater. *11*, 789–799. https://doi.org/10.1039/d2ta07655a.
46. Lin, B., Liu, Y., Heng, L., Wang, X., Ni, J., Lin, J., and Jiang, L. (2018). Morphology Effect of Ceria on the Catalytic Performances of Ru/CeO_2 Catalysts for Ammonia Synthesis. Ind. Eng. Chem. Res. *57*, 9127–9135. https://doi.org/10.1021/acs.iecr.8b02126.
47. Wang, R., Wang, Y., Ren, M., Sun, G., Gao, D., Chin Chong, Y.R., Li, X., and Chen, G. (2017). Effect of ceria morphology on the catalytic activity of Ru/ceria for the dehydrogenation of ammonia borane. Int. J. Hydrogen Energy *42*, 6757–6764. https://doi.org/10.1016/j.ijhydene.2017.02.024.
48. He, L., Ren, Y., Fu, Y., Yue, B., Tsang, S., and He, H. (2019). Morphology-dependent catalytic activity of Ru/CeO_2 in dry reforming of methane. Molecules *24*, 526–612. https://doi.org/10.3390/molecules24030526.
49. Li, X., Liu, X., Hao, J., Li, L., Gao, Y., Gu, Y., Cao, Z., and Liu, J. (2022). Strong Metal-Support Interactions of Ni-CeO_2 Effectively Improve the Performance of a Molten Hydroxide Direct Carbon Fuel Cell. ACS Omega *7*, 24646–24655. https://doi.org/10.1021/acsomega.2c02479.
50. Barroso-Bogeat, A., Blanco, G., Pérez-Sagasti, J.J., Escudero, C., Pellegrin, E., Herrera, F.C., and Pintado, J.M. (2021). Thermocatalytic CO_2 conversion over a

nickel-loaded ceria nanostructured catalyst: A NAP-XPS study. Materials *14*, 1–19. https://doi.org/10.3390/ma14040711.

51. Oliveira, M.E.R., Nobre, F.X., Dos Santos, J.R., and De Matos, J.M.E. (2017). The influence of a nickel precursor on the synthesis of nanosized NiO material using the hydrothermal method: Characterization and electrocatalytic oxidation of methanol. Mater. Sci. Forum *881 MSF*, 464–470. https://doi.org/10.4028/www.scientific.net/MSF.881.464.
52. Yang, Y., Ren, Y., Sun, C., and Hao, S. (2014). Facile route fabrication of nickel based mesoporous carbons with high catalytic performance towards 4-nitrophenol reduction. Green Chem. *16*, 2273–2280. https://doi.org/10.1039/c3gc42121j.
53. Chalupczok, S., Kurzweil, P., Hartmann, H., and Schell, C. (2018). The Redox Chemistry of Ruthenium Dioxide: A Cyclic Voltammetry Study—Review and Revision. Int. J. Electrochem. *2018*, 1–15. https://doi.org/10.1155/2018/1273768.
54. Cabañas-Polo, S., Ferrari, B., Gordo, E., Sánchez-Herencia, A.J., and Argirusis, C. (2012). Nanosized Nickel Powders Synthesized by a Reduction Method Assisted by Ultrasound. In Proceedings of the International Euro Powder Metallurgy Congress and Exhibition, *2012* (Euro PM), pp. 23–26.
55. González-Cruz, R., Solorza-Feria, O., González-Huerta, R.G., González-Cruz, R., Citalán-Cigarroa, S., Montero-Ocampo, C., and Chavez-Carvayar, J. (2005). Development and Electrochemical Studies of Ruthenium Nanoparticles as Cathode in a PEMFC. J. N. Mater. Electrochem. Syst. *8*, 15–23.
56. Wu, T.S., Zhou, Y., Sabirianov, R.F., Mei, W.N., Soo, Y.L., and Cheung, C.L. (2016). X-ray absorption study of ceria nanorods promoting the disproportionation of hydrogen peroxide. Chem. Commun. *52*, 5003–5006. https://doi.org/10.1039/c5cc10643e.
57. Tiwari, S., Rathore, G., Patra, N., Yadav, A.K., Bhattacharya, D., Jha, S.N., Tseng, C.M., Liu, S.W., Biring, S., and Sen, S. (2019). Oxygen and cerium defects mediated changes in structural, optical and photoluminescence properties of Ni substituted CeO_2. J. Alloys Compd. *782*, 689–698. https://doi.org/10.1016/j.jallcom.2018.12.009.
58. Phokha, S., Swatsitang, E., and Maensiri, S. (2015). Room-temperature ferromagnetism in pure CeO_2 nanoparticles prepared by a simple direct thermal decomposition. Electron. Mater. Lett. *11*, 1012–1020. https://doi.org/10.1007/s13391-015-4164-4.
59. Fernandes, V., Graff, I.L., Varalda, J., Amaral, L., Fichtner, P., Demaille, D., Zheng, Y., Schreiner, W.H., and Mosca, D.H. (2011). Valence Evaluation of Cerium in Nanocrystalline CeO_2 Films Electrodeposited on Si Substrates. J. Electrochem. Soc. *159*, K27–K33. https://doi.org/10.1149/2.056201jes.
60. Ranasinghe, K.S., Singh, R., Day, D.E., Attenkofer, K., Stavitski, E., Quinn, L.A., Patterson, D., and Duenas, A. (2019). Evidence of the coexistence of multivalence cerium oxide nano-particles in a sodium borate glass. J. Non-Cryst. Solids *515*, 75–81. https://doi.org/10.1016/j.jnoncrysol.2019.04.001.
61. Paidi, V.K., Brewe, D.L., Freeland, J.W., Roberts, C.A., and van Lierop, J. (2019). Role of Ce 4f hybridization in the origin of magnetism in nanoceria. Phys. Rev. B *99*, 180403. https://doi.org/10.1103/PhysRevB.99.180403.
62. Chen, Y., Okur, H.I., Lütgebaucks, C., Roke, S., Zhao, B., Wei, Y., Zhang, L., Yoo, S., Pei, K., Kim, J.H., et al. (2018). Zwitterionic and Charged Lipids Form Remarkably Different Structures on Nanoscale Oil Droplets in Aqueous Solution. Langmuir *34*, 1042–1050. https://doi.org/10.1038/s41560-018-0262-5.
63. Mullins, D.R., Overbury, S.H., and Huntley, D.R. (1998). Electron spectroscopy of single crystal and polycrystalline cerium oxide surfaces. Surf. Sci. *409*, 307–319. https://doi.org/10.1016/S0039-6028(98)00257-X.
64. Davidson, A., Tempere, J.F., Che, M., Roulet, H., and Dufour, G. (1996). Spectroscopic studies of nickel(II) and nickel(III) species generated upon thermal treatments of nickel/ceria-supported materials. J. Phys. Chem. *100*, 4919–4929. https://doi.org/10.1021/jp952268w.
65. Roy, B., and Leclerc, C.A. (2015). Study of preparation method and oxidization/reduction effect on the performance of nickel-cerium oxide catalysts for aqueous-phase reforming of ethanol. J. Power Sources *299*, 114–124. https://doi.org/10.1016/j.jpowsour.2015.08.069.
66. Mansour, A.N., and Melendres, C.A. (1994). Characterization of Ni_2O_3–$6H_2O$ by XPS. Surf. Sci. Spectra *3*, 263–270. https://doi.org/10.1116/1.1247755.
67. Biesinger, M.C., Payne, B.P., Grosvenor, A.P., Lau, L.W., Gerson, A.R., and Smart, R.S. (2011). Resolving surface chemical states in XPS analysis of first row transition metals, oxides and hydroxides: Cr, Mn, Fe, Co and Ni. Appl. Surf. Sci. *257*, 2717–2730. https://doi.org/10.1016/j.apsusc.2010.10.051.
68. Morgan, D.J. (2015). Resolving ruthenium: XPS studies of common ruthenium materials. Surf. Interface Anal. *47*, 1072–1079. https://doi.org/10.1002/sia.5852.
69. Matienzo, J., Yin, L.I., Grim, S.O., and Swartz, W.E. (1973). X-Ray Photoelectron Spectroscopy of Nickel Compounds. Inorg. Chem. *12*, 2762–2769. https://doi.org/10.1021/ic50130a005.
70. Bianchi, C.L., Ragaini, V., and Cattania, M.G. (1991). An XPS study on ruthenium compounds and catalysts. Mater. Chem. Phys. *29*, 297–306.
71. Elmasides, C., Kondarides, D.I., Grünert, W., and Verykios, X.E. (1999). XPS and FTIR Study of Ru/Al_2O_3 and Ru/TiO_2 Catalysts: Reduction Characteristics and Interaction with a Methane−Oxygen Mixture. J. Phys. Chem. B *103*, 5227–5239. https://doi.org/10.1021/jp9842291.
72. Huang, H., Dai, Q., and Wang, X. (2014). Morphology effect of Ru/CeO_2 catalysts for the catalytic combustion of chlorobenzene. Appl. Catal., B *158–159*, 96–105. https://doi.org/10.1016/j.apcatb.2014.01.062.
73. Fifere, N., Airinei, A., Dobromir, M., Sacarescu, L., and Dunca, S.I. (2021). Revealing the effect of synthesis conditions on the structural, optical, and antibacterial properties of cerium oxide nanoparticles. Nanomaterials *11*, 2596. https://doi.org/10.3390/nano11102596.
74. Koshtyal, Y., Nazarov, D., Ezhov, I., Mitrofanov, I., Kim, A., Rymyantsev, A., Lyutakov, O., Popovich, A., and Maximov, M. (2019). Atomic layer deposition of NiO to produce active material for thin-film lithium-ion batteries. Coatings *9*, 301. https://doi.org/10.3390/coatings9050301.
75. Wang, W., Guo, S., Lee, I., Ahmed, K., Zhong, J., Favors, Z., Zaera, F., Ozkan, M., and Ozkan, C.S. (2014). Hydrous ruthenium oxide nanoparticles anchored to graphene and carbon nanotube hybrid foam for supercapacitors. Sci. Rep. *4*, 4452. https://doi.org/10.1038/srep04452.
76. He, X., Liu, B., Zhang, S., Li, H., Liu, J., Sun, Z., and Chang, H. (2022). Nickel Nitrate Hydroxide Holey Nanosheets for Efficient Oxygen Evolution Electrocatalysis in Alkaline Condition. Electrocatalysis *13*, 37–46. https://doi.org/10.1007/s12678-021-00686-3.
77. Rojas, J.V., Toro-Gonzalez, M., Molina-Higgins, M.C., and Castano, C.E. (2016). Facile radiolytic synthesis of ruthenium nanoparticles on graphene oxide and carbon nanotubes. Mater. Sci. Eng., B *205*, 28–35. https://doi.org/10.1016/j.mseb.2015.12.005.
78. Jacobs, G., Patterson, P.M., Williams, L., Sparks, D., and Davis, B.H. (2004). Low temperature water-gas shift: role of pretreatment on formation of surface carbonates and formates. Catal. Lett. *96*, 97–105. https://doi.org/10.1023/B:CATL.0000029536.52909.92.
79. Zheng, W., Zhang, J., Ge, Q., Xu, H., and Li, W. (2008). Effects of CeO_2 addition on Ni/Al_2O_3 catalysts for the reaction of ammonia decomposition to hydrogen. Appl. Catal., B *80*, 98–105. https://doi.org/10.1016/j.apcatb.2007.11.008.
80. Gennequin, C., Poupin, C., Abi-Aad, E., Mahfouz, R., Aouad, S., and Estephane, J. (2020). CO_2 Methanation over Ru and/or Ni based catalysts Osupported on KIT-6, Al_2O_3 and CeO_2. In 11th International Renewable Energy Congress, IREC 2020 (Institute of Electrical and Electronics Engineers Inc), pp. 1–5. https://doi.org/10.1109/IREC48820.2020.9310374.
81. Li, J., Liu, Z., Cullen, D.A., Hu, W., Huang, J., Yao, L., Peng, Z., Liao, P., and Wang, R. (2019). Distribution and Valence State of Ru Species on CeO_2 Supports: Support Shape Effect and Its Influence on CO Oxidation. ACS Catal. *9*, 11088–11103. https://doi.org/10.1021/acscatal.9b03113.
82. Hossain, M.Z., Chowdhury, M.B., Alsharari, Q., Jhawar, A.K., and Charpentier, P.A. (2017). Effect of mesoporosity of bimetallic Ni-Ru-Al_2O_3 catalysts for hydrogen production during supercritical water gasification of glucose. Fuel Process. Technol. *159*, 55–66. https://doi.org/10.1016/j.fuproc.2017.01.013.
83. Liu, Y., Wu, Y., Akhtamberdinova, Z., Chen, X., Jiang, G., and Liu, D. (2018). Dry Reforming of Shale Gas and Carbon Dioxide with Ni-Ce-Al_2O_3 Catalyst: Syngas Production Enhanced over Ni-CeO_x Formation. ChemCatChem *10*, 4689–4698. https://doi.org/10.1002/cctc.201800829.
84. Kim, E.J., Woo Kim, Y., Wan Kim, T., Suh, Y.W., Shin, C.H., An, K., and Min, H.K. (2023). Hydrogen production by the catalytic decomposition of ammonia over a Ru/$SiCeO_x$ catalyst: The synergistic effect of Si addition. Fuel *354*, 129293. https://doi.org/10.1016/j.fuel.2023.129293.
85. Le, T.A., Kim, Y., Kim, H.W., Lee, S.U., Kim, J.R., Kim, T.W., Lee, Y.J., and Chae, H.J. (2021). Ru-supported lanthania-ceria composite as an efficient catalyst for CO_x-free H_2 production from ammonia decomposition. Appl. Catal., B *285*, 119831. https://doi.org/10.1016/j.apcatb.2020.119831.
86. Al-Shafei, E.N., Albahar, M.Z., Albashrayi, R., Aljishi, M., Alasseel, A., Tanimu, G., and Aitani,

A. (2023). The effect of acidic–basic structural modification of nickel-based catalyst for ammonia decomposition for hydrogen generation. Mol. Catal. *550*, 113581. https://doi.org/10.1016/j.mcat.2023.113581.

87. Li, H., Guo, L., Qu, J., Fang, X., Fu, Y., Duan, J., Wang, W., and Li, C. (2023). Co-Ni supported yttrium oxide material as a catalyst for ammonia decomposition to CO_x-free hydrogen. Int. J. Hydrogen Energy *48*, 8985–8996. https://doi.org/10.1016/j.ijhydene.2022.11.338.

88. Zhang, T., Ju, X., Liu, L., Liu, L., He, T., Xu, Y., Wang, H., and Chen, P. (2023). Steering ammonia decomposition over Ru nanoparticles on ZrO_2 by enhancing metal-support interaction. Catal. Sci. Technol. *13*, 5205–5213. https://doi.org/10.1039/d3cy00691c.

89. Ravel, B., and Newville, M. (2005). ATHENA, ARTEMIS, HEPHAESTUS: Data analysis for X-ray absorption spectroscopy using IFEFFIT. J. Synchrotron Radiat. *12*, 537–541. https://doi.org/10.1107/S0909049505012719.

STAR★METHODS

KEY RESOURCES TABLE

REAGENT or RESOURCE	SOURCE	IDENTIFIER
Chemicals, peptides, and recombinant proteins		
NH_3 (28 vol. %)	Scharlab	AM02562500
$Ce(NO_3)_3 \cdot 6H_2O$	Alfa Aesar	11361089
$Ni(CH_3COO)_2 \cdot 4H_2O$	Probus	Not available
$Ni(NO_3)_2 \cdot 6H_2O$	Thermo Fisher Scientific	A15540.0B
$RuCl_3$	Tokyo Chemical Industries	R0074
$Ru(CH_3COO)_3$	Biosynth	3D-XCA19632
Ru nanoparticles	Sigma Aldrich	326712-1G
Ni nanoparticles	Sigma Aldrich	577995-5G

RESOURCE AVAILABILITY

Lead contact

Further information and requests for resources and reagents should be directed to and will be fulfilled by the lead contact, Jordi Llorca (jordi.llorca@upc.edu).

Materials availability

No new reagents were created in the presented research.

Data and code availability

- All data reported in this paper will be shared by the lead contact upon request.
- This paper does not report original code.
- Any additional information required to reanalyze the data reported in this paper is available from the lead contact upon request.

METHOD DETAILS

Preparation of catalysts

CeO_2 was prepared by adding NH_3 (28 vol. %, *Scharlab*) to a magnetically stirred solution of $Ce(NO_3)_3 \cdot 6H_2O$ (*Alfa Aesar*) in water, until pH~9. The precipitate was filtered (with a porous plate n° 4) and calcined at 500°C (4 h, 5°C min^{-1}). All prepared catalysts have a content of 5 wt.% Ni and 1 wt.% Ru. The catalysts synthesized using the incipient wetness impregnation (IWI) method were prepared by co-impregnation with an aqueous solution of Ni and Ru precursors. Between each impregnation phase the catalyst is dried at 100°C for approximately 10 min and ground. After the impregnation, the catalysts were dried at 100°C for 24 h, ground, and then calcined at 450°C for 4 h using a ramp of 5°C min^{-1}. The monometallic counterparts were prepared following the same method, but dissolving only the respective precursor in distilled water. The precursors that were used for IWI catalysts are $Ni(CH_3COO)_2 \cdot 4H_2O$ (*Probus*) and $Ni(NO_3)_2 \cdot 6H_2O$ (*Thermo Fisher Scientific*) for Ni, while those for Ru were $RuCl_3$ (*Tokyo Chemical Industries*) and $Ru(CH_3COO)_3$ (*Biosynth*). The catalysts synthesized using the mechanochemical (MM) method were prepared employing a moderate-energy vibrating ball mill (Pulverisette 23, *FRITSCH*). Ceria and the chosen Ni and Ru precursors were loaded into a 15 mL zirconia vial equipped with a 15 mm diameter high wear-resistant zirconia ball. The vial was agitated at an oscillation frequency of 15 Hz for 10 min, with a ball/powder ratio of 8.5/1. The same precursors used for the IWI method were also employed for the catalysts prepared with the MM method, however, in this case, Ru nanoparticles (*Sigma Aldrich*) and Ni nanoparticles (*Sigma Aldrich*) were also used. The monometallic counterparts were prepared following the same method, introducing in the vial only the corresponding precursor and ceria. Furthermore, a comparison was made by introducing the precursors into the vial in two steps: in a first step the first precursor and CeO_2 were milled together, followed by the addition of the second precursor in a subsequent step. For these catalysts the same milling conditions were used, varying the total time and both steps lasted 10 min. The nomenclature of the catalysts was defined by indicating the type of precursors (nitrate: N, acetate: A, chloride: C and nanoparticles: np). In the case of the two-step preparation, this was indicated with a line between the two precursors, starting with the precursor used in the first phase. Finally, the method used was specified by adding IWI or MM at the end.

Catalyst characterization techniques

High-resolution transmission electron microscopy (HRTEM) images were acquired in a field emission gun FEI *Tecnai* F20 microscope operated at 200 kV. The crystal structure was analyzed using the frequency spots in the corresponding fast Fourier transformations (FFTs) using

Gatan Digital Micrograph software. The HAADF images and EDX maps were acquired in a double corrected and monochromated *Thermo Fisher* Spectra 300 microscope operated at 300 kV using scanning transmission electron microscopy (STEM) mode. The HAADF images and EDX maps have been analyzed by Velox software. Raman spectroscopy was performed with a *Renishaw* inVia Qontor confocal Raman microscope (532.1 nm laser) and a *Leica* DM2700 M microscope (×50). An exposure time of 0.5 s and 12 repetitions were used to acquire the spectra. *Ex situ* X-ray absorption spectroscopy (XAS) and X-ray diffraction (XRD) analysis were conducted at the NOTOS beamline of the ALBA Synchrotron Light Source facility (Cerdanyola del Vallès, Barcelona, Spain). The synchrotron light coming from a bending magnet has been first vertically collimated, then monochromatized using two pairs of water-cooled Si(111) crystals and finally focused on the sample position down to ~500 × 500 μm^2. Si and Rh stripe coatings of the two mirrors were opportunely chosen to guarantee the higher harmonics rejection. The beamline was initially set to an energy configuration capable of exciting Ce atoms around the Ce L_3-edge (5723 eV) and the samples were measured in transmission mode using three DC current-type ionization chambers (I0, I1 and I2, where a reference is placed between the chambers I1 and I2, *Oken*) filled with the appropriate mixture of inert gases. Subsequently, Ni was analyzed by changing the configuration to excite the Ni atoms around its K-edge (8333 eV) and the samples were measured in fluorescence (13-element Si detector, *Canberra*). For Ru fluorescence measurement, the setup was modified using the Rh stripe to reach the high energies required by its K-edge (22117 eV). Just before the Ru K absorption edge, XRD diffractograms were recorded at 21000 eV using a Mythen-I detector (*Dectris*) in a 2θ range of 42°, measuring with three different detector positions for 5 s each. All catalysts were analyzed in pellet form, and prepared by diluting the sample with cellulose. A minimum of three extended X-ray absorption fine structure spectra (EXAFS) were acquired to ensure spectral reproducibility and a good signal-to-noise ratio. Data analysis and treatment were conducted using the *Demeter* software package.[89] The Fourier Transform (FT) was obtained on k^2-weighted EXAFS oscillations in the range of 2.9–10.8 $Å^{-1}$ and R space range of 0–6 Å. The average crystallite size, denoted as *L* [nm], was calculated from the highest intensity peak from XRD patterns using the Debye-Scherrer equation (Equation 1):

$$L = \frac{K\lambda}{\beta \cos \gamma} \quad \text{(Equation 1)}$$

Where 0.89 was chosen for the shape factor *K*, λ [nm] is the wavelength, β [rad] is the full width at half maximum (FWHM), and γ [rad] is the Bragg angle.

X-ray photoelectron spectroscopy (XPS) analysis utilized a *SPECS* system equipped with a *PHOIBOS* 150 EP Hemispherical Energy Analyzer with an MCD-9 detector, using a Mg Kα X-ray source of 1253.6 eV energy and 150 W power, and a pass energy of 20 eV. The X-ray source is placed at 54° with respect to the analyzer axis and is calibrated by using the Ag $3d_{5/2}$ line with a full width at half maximum of 1.211 eV. A flood gun operating at 15 μA and 1.5 eV was used to compensate the charge. The measurements were calibrated against the C 1s peak at a binding energy (BE) of 284.7 eV and the U‴ Ce 3days peak at 916.9 eV. CasaXPS software (*Casa Software Ltd.*, Teignmouth, UK) was employed for result analysis. Atomic fractions were estimated by normalizing peak areas based on acquisition parameters following background subtraction, experimental sensitivity factors, and the analyzer transmission efficiency provided by the manufacturer. H_2-temperature programmed reduction (H_2-TPR) experiments were conducted using a *Chemstar-TPX* instrument equipped with a Thermal Conductivity Detector (TCD). Initially, 50 mg of the sample were heated from room temperature (RT) to 450°C in an argon flow rate of 50 mL min^{-1}, with a heating rate of 10 °C min^{-1}. Then the samples were maintained at 450°C for 10 min, before being cooled down to 50°C under an argon flow. Subsequently, H_2-TPR was carried out from 50°C to 850°C at a rate of 10 °C min^{-1} in a mixture of 10% H_2 in Ar, with a total flow rate of 50 mL min^{-1}. The samples were then held at 500°C for 30 min.

Catalytic tests

Ammonia decomposition experiments were conducted in a stainless-steel reactor under atmospheric pressure conditions. 0.1 g of the catalyst were combined with SiC to achieve a bed volume of approximately 0.41 cm^3. Temperature-dependent tests for the reaction were performed within the temperature range of 350°C–600ºC, at steps of 50°C, each lasting 30 min. The blank test was performed without any catalyst using the same volume of SiC. Stability tests were conducted for 100 h at 450°C. The gas mixture used had an Ar:NH_3 molar ratio of 1.2:1, and the total gas flow rate was set at 25 mL min^{-1}. The control of the gas flow was achieved using *Bronkhorst* mass flow controllers. Before starting the catalytic tests, the samples were activated at 300°C for 1 h in a 10 vol. % H_2 atmosphere (80 mL min^{-1}, N_2 balance). The reaction progress was continuously monitored using a mass spectrometer (*OmniStar)* with a measurement error of ±5%. Ammonia conversion (denoted as *x* [%]) was determined using Equation 2 using the inlet and outlet molar flow rates of ammonia, F_{inNH3} and F_{outNH3}, respectively (measured in mol NH_3 s^{-1}).

$$x = \frac{F_{inNH_3} - F_{outNH_3}}{F_{inNH_3}} \times 100 \quad \text{(Equation 2)}$$

QUANTIFICATION AND STATISTICAL ANALYSIS

The standard deviation of the particle size measured from TEM images (Figure 1) is estimated by determining the width of the Gaussian curve when the frequency is half of the maximum value, and then dividing it width by 2.

In *Demeter* software package, *Athena* uses Least Squares Method for XANES spectra fitting (Table 1) and linear combination analysis (Table 2).